

Analysis of tidal flows through the Strait of Gibraltar using Dynamic Mode Decomposition

Sathsara Dias^a, Sudam Surasinghe^{a,b}, Kanaththa Priyankara^{a,c}, Marko Budišić^a, Larry Pratt^d, José C. Sanchez-Garrido^e, Erik M. Bollt^f

^a*Department of Mathematics, Clarkson University, 8 Clarkson Ave, 13699, Potsdam, NY, United States of America*

^b*Department of Ecology & Evolutionary Biology, Yale University, 165 Prospect Street, 06511, New Haven, CT, United States of America*

^c*Alabama A&M University, 4900 Meridian St N, 35811, Huntsville, AL, United States of America*

^d*Woods Hole Oceanographic Institution, 266 Woods Hole Road MS#21, 02543-1535, Woods Hole, MA, United States of America*

^e*Universidad de Málaga, Avda. Cervantes 2, 29071, Málaga, Spain*

^f*Department of Electrical and Computer Engineering, Clarkson University, 8 Clarkson Ave, 13699, Potsdam, NY, United States of America*

Abstract

The Strait of Gibraltar is a region characterized by intricate oceanic sub-mesoscale features, influenced by topography, tidal forces, instabilities, and nonlinear hydraulic processes, all governed by the nonlinear equations of fluid motion. In this study, we aim to uncover the underlying physics of these phenomena within 3D MIT general circulation model simulations, including waves, eddies, and gyres. To achieve this, we employ Dynamic Mode Decomposition (DMD) to break down simulation snapshots into Koopman modes, with distinct exponential growth/decay rates and oscillation frequencies. Our objectives encompass evaluating DMD's efficacy in capturing known features, unveiling new elements, ranking modes, and exploring order reduction. We also introduce modifications to enhance DMD's robustness, numerical accuracy, and robustness of eigenvalues. DMD analysis yields a comprehensive understanding of flow patterns, internal wave formation, and the dynamics of the Strait of Gibraltar, its meandering behaviors, and the formation of a secondary gyre, notably the Western Alboran Gyre, as well as the propagation of Kelvin and coastal-trapped waves along the African coast. In doing so, it significantly advances our comprehension of intricate oceanographic phenomena and underscores the immense utility of DMD as an analytical tool for such complex datasets, suggesting that DMD could serve as a valuable addition to the toolkit of oceanographers.

Keywords: Dynamic Mode Decomposition (DMD); Koopman Operator; Strait of Gibraltar; Oceanic flow; Feature Analysis; Enhancing Robustness and Numerical Accuracy of DMD; Kernel Density Estimates (KDE) for Mode Selection.

Contents

Symbols	2
1 Introduction	3
2 Model of ocean dynamics in the Strait of Gibraltar	5
2.1 Oceanographic features in the region	5
2.2 Numerical model and the analyzed data	6
3 Dynamic Mode Decomposition of the simulated flow	11
3.1 Representing dynamics using the Koopman operator	11
3.2 Dynamic Mode Decomposition as numerical Koopman analysis	14
3.3 Improving interpretability, stability, and robustness	17
4 Analysis of the DMD spectrum and DMD modes	20
4.1 SVD subspace selection	20
4.2 Robustness of eigenvalues	22
4.3 Contributions of individual modes	23
4.4 Low-rank model of simulated data	27
5 Connections between modes and oceanographic features	28
5.1 Western Alboran Gyre and secondary gyres	29
5.2 Oscillation inside the Strait	30
5.3 Meanders in the Atlantic Jet	32
5.4 Kelvin waves along the African coast	33
6 Discussion and conclusions	36
7 Acknowledgments	38

Symbols

\mathbb{K}	Koopman operator
\mathbb{S}	evolution operator
\mathbf{K}	DMD matrix
$\tilde{\mathbf{K}}$	Reduced-order DMD matrix
μ	Koopman (discrete-time) eigenvalue
λ	Koopman (continuous-time) eigenvalue

- ρ Koopman (continuous-time) decay rate
- ω Koopman (continuous-time) ang. frequency
- τ Doubling time (negative sign indicates halving time)
- P Period of oscillation
- Φ Koopman eigenmode
- Ψ Koopman eigenfunction
- b Coefficients in Koopman decomposition
- $\tilde{\Phi}$ Reduced-order eigenmode
- \tilde{b} RMS of mode norm
- ${}_w b$ Coefficients in Koopman decomposition
- ${}_w \tilde{b}$ RMS of mode norm restricted to vertical velocities

1. Introduction

The interpretation of geophysical data often involves a search for dominant features or physical processes. Examples include spatial distributions dominated by a small number of empirical orthogonal functions, vertical structure dominated by the lowest few vertical dynamical modes, processes responsible for peaks in energy spectra, or multiscale phenomena describable by simple scaling laws. Once such a feature is identified, it may be possible to gain deeper insight through examination using reduced order models, including idealized models grounded in the governing equations of motion or models that are constructed entirely from field data or data generated by large models of general circulation and climate.

Dynamic Mode Decomposition (DMD) [1, 2] and its various iterations have, over the past decade, been shown to identify dominant, interpretable features of a data set that lead to low-order, linear models describing the time evolution of the features. Among other competing approaches, such as Proper Orthogonal Decomposition (POD) [3], Empirical Orthogonal Functions (EOF) [4, 5] and others (see [6, 7] for modern comparative reviews), DMD has been distinguished by an interpretation that casts it as an approximation of the more general framework employing the linear Koopman operator for analysis of nonlinear dynamical systems [8–13] or, simply, Koopman analysis.

Conceptually, Koopman analysis augments the set of variables on which the model depends by a set of variables computed by *all* functions on the original state space (*observables*). As a consequence, any nonlinear term present in the original equations is given its own “synthetic” variable; as this leads to an explosion of variables, the effect is that

the linearity of the model is obtained in return for the dimension of the model growing. At first glance, transformation to a linear system of infinite order would appear to be the opposite of order reduction, but hope is that the infinite set can be represented to a good approximation by a large, but finite, dynamical system and that the solutions will exhibit low-order behavior. The numerical algorithms, like those in the DMD family, strive to compute eigenvalues and eigenvectors of this linear, infinite-dimensional linear system without explicitly trying to reconstruct its system matrix. The computed eigenvalues indicate the character of time variation of individual components: their interpretation is the same as in basic stability theory of linear systems. The eigenvectors approximate Koopman modes whose interpretation depends on the choice of observed variables; when input variables are measurements of velocities in the computational domain, as is common in fluid mechanics, Koopman modes correspond to spatial profiles that grow, decay, and/or oscillate according to a single complex frequency (Koopman eigenvalue).

Since the seminal publication that first connected Schmid's DMD with Koopman analysis [2], many iterations of the DMD algorithm have been developed with standard goals common to many numerical algorithms such as improved robustness, improved efficiency, reduction of bias and noise, and improved convergence properties. Several reviews and edited volumes address various aspects of the interaction between Koopman analysis, numerics, and applications [12, 14–16]. While the proliferation of algorithms and applications lead to significant improvements on the original technique, it made it more challenging for those looking to test or adapt these algorithm to find an entry point.

Applications of DMD to fluid mechanics are arguably best studied, as early papers focused primarily on demonstrating the DMD on simulated fluid systems, typically in aerodynamic flows. However, DMD has not been applied to large oceanographic data sets, either those including models or observations.

The central goal of our work is to determine how well DMD works when applied to a region of the ocean that exhibits a variety of time-dependent, 3D physical features including waves, eddies, and gyres, some of which are generated by strongly nonlinear processes. How well do the Koopman modes capture the features that we already know about, and does the method reveal features that we do not know about? It is of additional interest to rank the numerous modes that are computed and determine what reduction in order can be achieved. Here we will discuss several alternatives.

The oceanic region selected includes the western Mediterranean Sea (Alboran Sea), the Strait of Gibraltar, and a portion of the Gulf of Cadiz as shown in Figure 1. The data consists of tide-resolving MITgcm output over a 6-day period and is detailed in Section 2. Prominent known features include the Western Alboran Gyre, the Atlantic Jet, the hydraulically controlled exchange flow in the Strait of Gibraltar, the time-dependent hydraulic jump that occurs to the west of the Camarinal Sill, and the internal waves that radiate eastward into the Mediterranean and are generated by the collapse of the hydraulic jump. The collapse is a strongly non-linear process caused by the flooding of the semi-diurnal tide into the Mediterranean Sea. Therefore, the standard harmonic analysis [17, 18] that consists of fit-

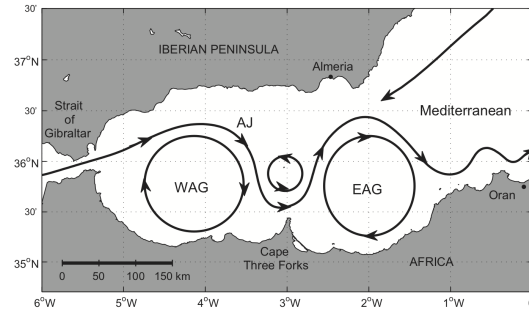
ting the data to a predetermined set of steady oscillation frequencies is not likely to capture the full breadth of dynamical behavior.

As a secondary goal, we aim to demonstrate how to apply the DMD to a data set in a straightforward and easy-to-implement fashion, while including several modern modifications aimed at improving numerical performance of the algorithm. We demonstrate how certain modeling choices affect the outcomes of the algorithm, whether by interpreting changes in individual DMD modes, or by evaluating the robustness and correctness of the reduced-order models in bulk.

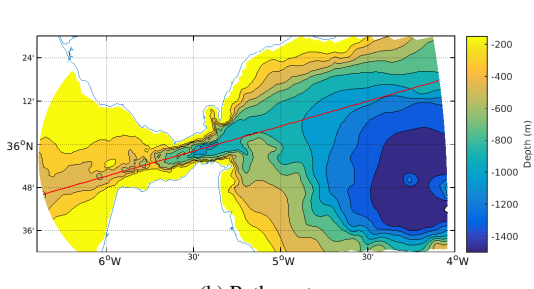
2. Model of ocean dynamics in the Strait of Gibraltar

2.1. Oceanographic features in the region

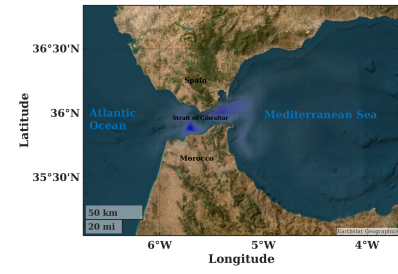
We focus our analysis on the region of the world roughly between -6.50 deg W and -4.00 deg W, and 35.00 deg N and 37.00 deg W, where the Atlantic Ocean and Mediterranean Sea, specifically the Gulf of Cádiz and the Western Alboran Sea, exchange water through the Strait of Gibraltar, as seen in Figure 1.



(a) Sketch of the Western Alboran Gyre (WAG) and the Atlantic Jet (AJ).



(b) Bathymetry .



(c) Topographic slice.

Figure 1: Topographic and oceanographic features of the regions near the Strait of Gibraltar. Slice in panel (c) is taken along the red line in panel (b). [19]

Among well-known oceanographic features, apparent in the of the mean flow, are the two-layer exchange flow in the strait, with a relatively fresh surface inflow and dense, salty

outflow at the bottom [20]. The exchange flow has been shown to be hydraulically controlled at the Camarinal Sill, the Espartel Sill and the Tarifa Narrows [21, 22]. The two-layer flow is also modulated by the tides and this has a dramatic impact near the Camarinal Sill where the outflowing Mediterranean layer spills, becomes hydraulically supercritical, and undergoes a turbulent hydraulic jump [23]. When the tide floods into the Mediterranean from the Atlantic, it can force the hydraulic jump to move eastward and eventually to the east side of Camarinal Sill, as seen in Section 2.1. There the jump collapses and develops into a set of soliton-like nonlinear internal waves that continue eastward and radiate into the Alboran Sea [21, 24–32]. Westward propagating internal waves have also been observed to the west of Camarinal Sill [21, 22, 29, 30], but these are less common. Waves released during different tides and seasons may differ, some propagating preferentially towards the northeast or the southeast. High-resolution numerical models suggest the presence of stationary internal waves within and around the strait, caused by flow over rough topography [33].

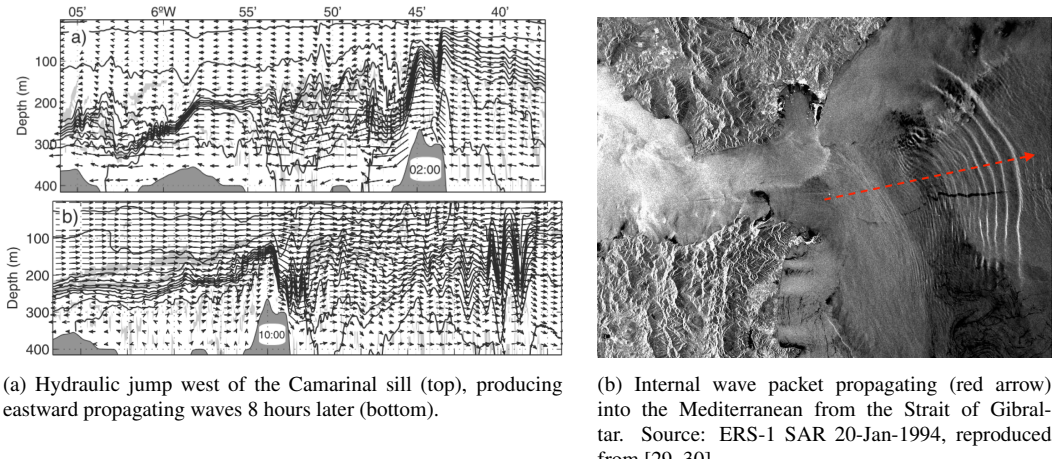


Figure 2: Hydraulic jump at the Camarinal sill generates eastward waves, with an internal wave packet entering the Mediterranean from the Strait of Gibraltar.

2.2. Numerical model and the analyzed data

The oceanic flow was simulated using the 3-D, finite-volume, MIT general circulation model (MITgcm [34]) applied to the ocean region of the Strait of Gibraltar ([35, 36]). The model domain covers the Alboran Sea and the Gulf of Cadiz (connected by the Strait of Gibraltar), and was discretized with a curvilinear orthogonal grid of variable resolution. Horizontal resolution varies from 0.5 km in the Strait itself (smallest mesh size) to 3-4 km towards the adjacent basins. In the vertical, the model incorporates 32 unevenly distributed z -levels with maximum resolution at the near surface ($\Delta z = 5$ m). The total size of the com-

putational grid is $190 \times 96 \times 32$. Simulations used 1h timestep over a 6d period, amounting to 144 snapshots of the simulation evolution.

Description	Symbol
Zonal velocity (Longitude-wise velocity component)	U_x
Meridional velocity (Latitude-wise velocity component)	U_y
Velocity along depth	U_z
Local horizontal speed	$U_s = \sqrt{U_x^2 + U_y^2}$
Time average of U_x	$\overline{U_x}$
Time average of U_y	$\overline{U_y}$
Time average of U_z	$\overline{U_z}$
Time average of U_s	$\overline{U_s}$
Magnitude/speed of the mean (time averaged) velocity vector	$S_{\overline{U}} = \sqrt{\overline{U_x}^2 + \overline{U_y}^2}$

Table 1: Summary of descriptions and symbols for velocity-related quantities as used throughout the article.

Vertical and horizontal subgrid mixing and dissipation was parameterized according to the K-profile [37] and Smagorinsky [38] turbulence schemes, respectively. At the surface, the model was driven by wind stress, heat fluxes and precipitation (fresh water flux) from NCEP/NCAR reanalysis [39]. Initial and lateral boundary values for temperature, salinity, and velocity current were extracted from CMEMS reanalysis products [40]. Astronomical forcing was also incorporated by adding barotropic tidal velocities to the velocity values calculated from CMEMS. The analysis in this article utilizes the velocity components and their magnitudes obtained from these numerical models. A summary of the descriptions and symbols employed for these velocity-related quantities throughout the article can be found in Table 1.

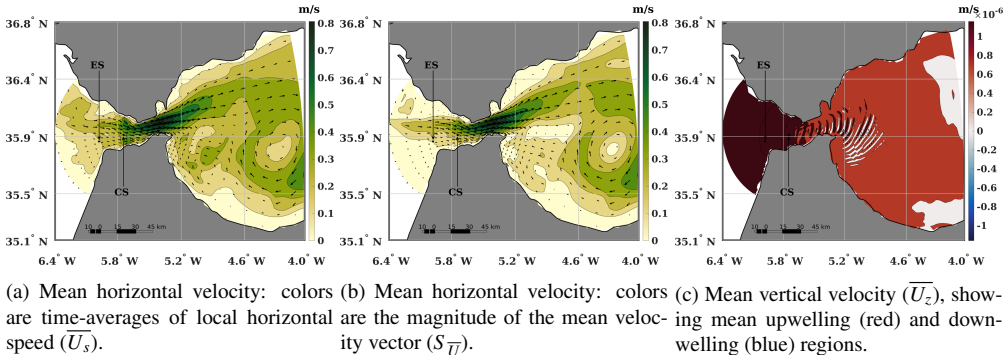
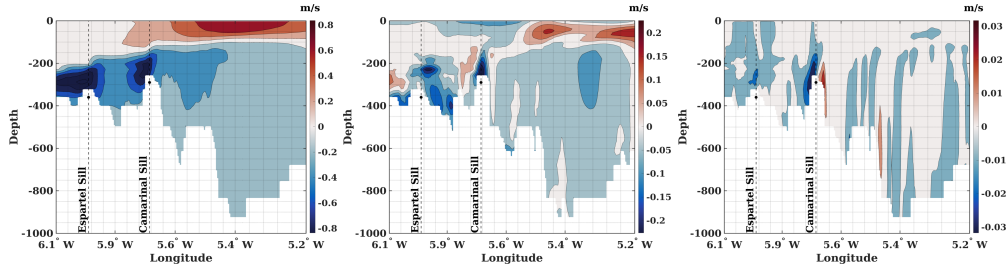


Figure 3: Average horizontal velocity [panels (a) and (b)] and vertical velocity [panel (c)] at the surface. Color in the first two panels shows that the mean speed vs. mean velocity heatmaps illustrate slightly different features, in particular the CCW gyre centered around -5.00° W, 35.50° N.



(a) Mean Zonal velocity component (U_x). (b) Mean Meridional velocity component (U_y). (c) Mean vertical (z-) velocity component (U_z).

Figure 4: Average velocity components along the vertical slice through the region. (see Figure 1).

Tides in the strait of Gibraltar are mainly semidiurnal [41, 42]. Analysis of acoustic Doppler observations [41] showed that as much as 96.00 % of the bottom pressure variability and 74.00 % of the current variability in the strait lie in the semidiurnal band. The most dominant semidiurnal tidal constituent is M2 followed in importance by S2. Reported tidal velocities at Camarinal sill are as large as 120 cm/s for M2 and 48 cm/s for S2 [43]. The diurnal band is dominated by the constituents K1 and O1, with associated velocities in the range of 15-35 m/s at Camarinal Sill [43]. Although most of the tidal energy is semidiurnal, diurnal currents are sufficiently strong to affect internal hydraulics. For example, during neap tides hydraulic control at Camarinal Sill is lost every two semidiurnal cycles (and not every tidal cycle) as a result of the diurnal inequality [44]. Consequently, only the principal semidiurnal (M2, S2, N2, K2) and diurnal (K1, O1, P1, Q1) tidal constituents, listed in Table 2, were included in the model. Further details and validation of the model results are available in [35, 36].

Figure 5 and Figure 6 give a sense of the major features in the evolution of the velocity field. In particular, the surface velocity shows the Western Alboran Gyre (WAG) and the Atlantic Jet (AJ), matching well with Figure 1, while the vertical slice shows the significant vertical velocity on the Mediterranean side of the Camarinal Sill, corresponding to the hydraulic jump. The spatial averages of speed show the dominant diurnal oscillation with a slight growth in amplitude over the simulated six-day window.

A notable feature of the exchange through the Strait of Gibraltar is the stratification of the flow into a denser, saltier Mediterranean water and the lighter, less-salty Atlantic water. The isohaline surface of 37.5ppm serves as an approximate boundary between the two, as the variation in the density of the seawater is primarily due to the concentration of salt. Since the numerical model produces the salinity field, we extract the time-varying 37.5ppm isohaline surface and compute its time-averaged depth (*mean-isohaline*) for each point in the longitude/latitude plane. The resulting surface, seen in Figure 7 still serves as an approximate dividing surface for the two layers within the strait. Visualizing outputs of the subsequent data analysis along this mean-isohaline will clarify the dynamics of the internal waves that propagate along the interface between the saltier and less-salty sea water.

Tidal Pattern	Symbol	P_{Td} [h]
Principal lunar semidiurnal	M_2	12.421
Principal solar semidiurnal	S_2	12.000
Larger lunar elliptic semidiurnal	N_2	12.658
Lunisolar semidiurnal	K_2	11.967
Lunar diurnal	K_1	23.935
Lunar diurnal	O_1	25.819
Solar diurnal	P_1	24.066
Larger lunar elliptic diurnal	Q_1	26.868
Smaller lunar elliptic diurnal	M_1	24.841
Lunar terdiurnal	M_3	8.280
Shallow water overtones of principal lunar	M_4	6.210
Shallow water overtones of principal lunar	M_6	4.140
Shallow water eighth diurnal	M_8	3.105
Solar diurnal	S_1	24.000

Table 2: The top portion of the table lists dominant tidal constituents [41] with their periods (P_{Td}) used in the tidal forcing of the model. The bottom portion are sub- and super-harmonics of the two principal components, which were not used explicitly in the forcing.

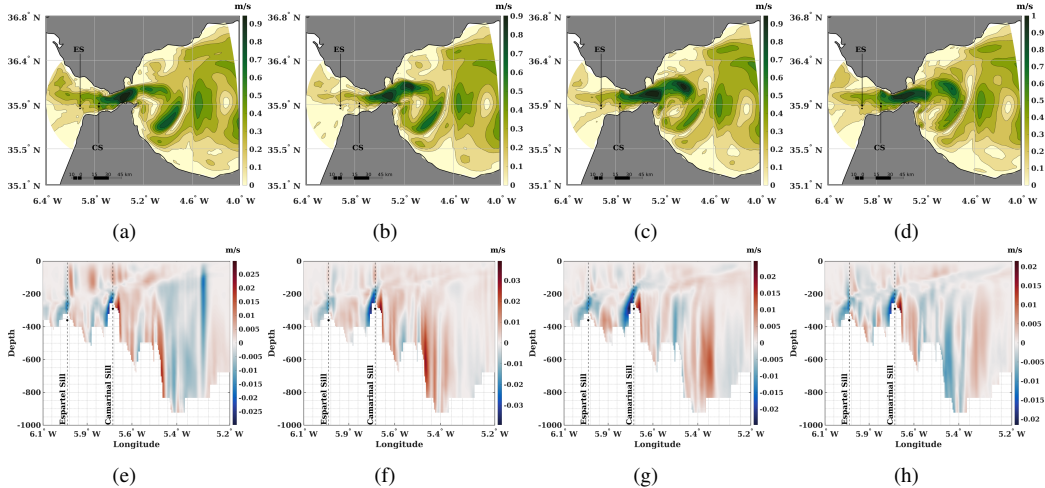


Figure 5: A semidiurnal period of the velocities. Snapshots of the horizontal speed $U_s = \sqrt{U_x^2 + U_y^2}$ at the surface layer (top row), and a slice through the vertical velocity (bottom row); frames progress from left to right at $t = 0\text{h}, 3\text{h}, 6\text{h}, 9\text{h}$.

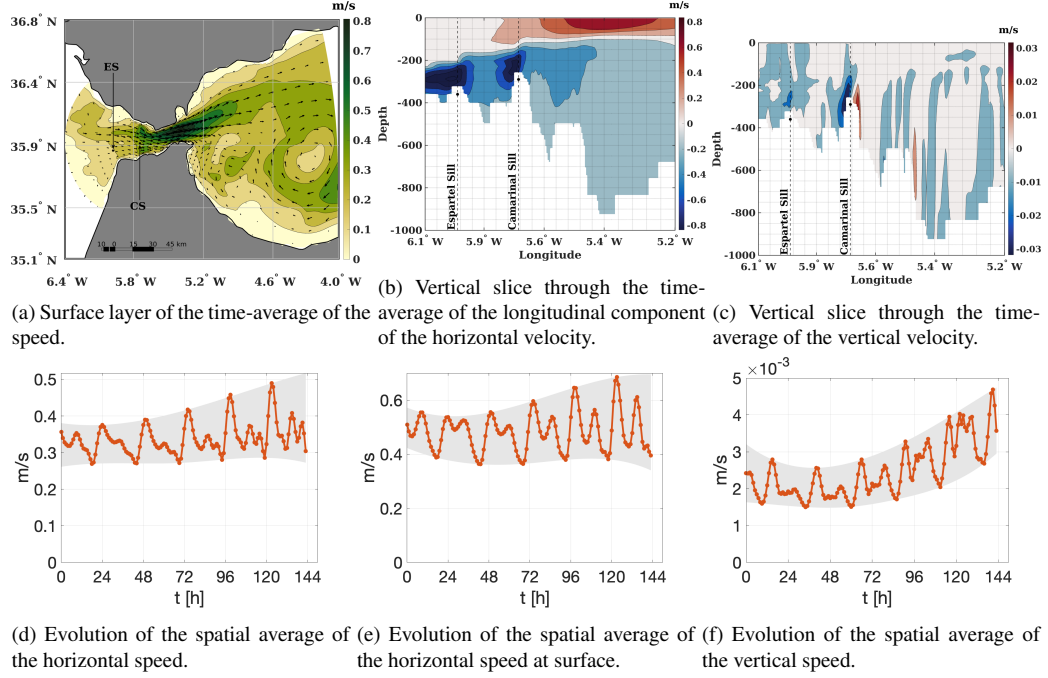


Figure 6: Time averages (top row) and space averages (bottom row) of the horizontal speed and the vertical velocity component. The shaded regions in the bottom row are the 24hour peak-to-peak envelope.

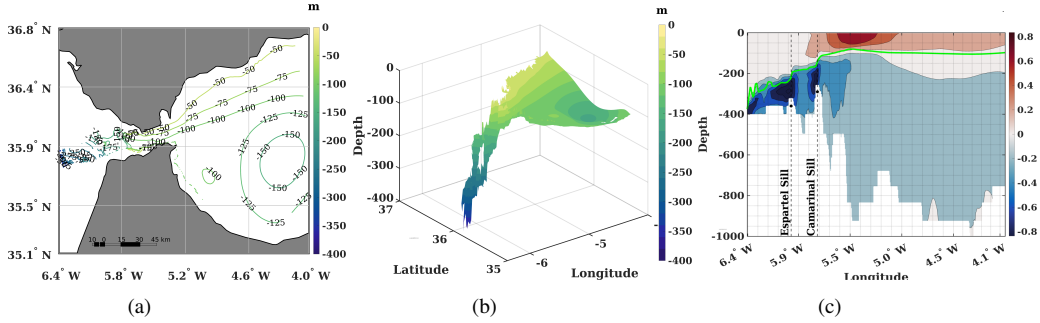


Figure 7: Mean depth of the 37.5ppm isohaline surface that serves as an approximate boundary between atlantic (lower density) and mediterranean waters (higher density).

3. Dynamic Mode Decomposition of the simulated flow

3.1. Representing dynamics using the Koopman operator

We start by summarizing the basic concepts of the “Koopmanism” approach to dynamical systems. To properly justify this approach, we have to disentangle the concept of “states of the system” and “observations of the system” which are often conflated in analysis of dynamical models, with notable exceptions of control theory and data assimilation literature. We present the basic concepts here without much theoretical justification, and point to [9, 12, 15] for more detail.

Consider a dynamical system over states $z \in \mathcal{Z}$

$$\frac{dz}{dt} = g(z) \quad (1)$$

In the context of our applications, states $z \in \mathcal{Z}$ correspond to all quantities necessary for evolution of the model equations. In general, they can be thought of as spectral coefficients if model equations are advanced by spectral solvers, grid-based evaluations of quantities in method-of-lines, etc. Almost always we assume that dimension of \mathcal{Z} is large, even infinite. As the time evolution is discretized into steps of duration Δt , states $z(n\Delta t)$ being evolved by a time-invariant, nonlinear solution operator $\mathbb{S}_0^{\Delta t} : \mathcal{Z} \rightarrow \mathcal{Z}$:

$$z[n] := z(n\Delta t) = \mathbb{S}_0^{\Delta t}(z[n-1]). \quad (2)$$

Since (1) was time invariant and as Δt remains fixed, we will write simply $\mathbb{S} := \mathbb{S}_0^{\Delta t} \equiv \mathbb{S}_t^{t+\Delta t}$.

Access to $z(t)$ is mediated by a vector of D observation functions $x : \mathcal{Z} \rightarrow \mathbb{R}^D$; therefore, we only have access to *snapshots*

$$\mathbf{X}[n] := x(z[n]) \quad \text{of} \quad \mathbf{X}(t) := x(z(t)). \quad (3)$$

In oceanography, simulations by general circulation models typically results in observation functions $x(\cdot)$ that are evaluations of velocity components, the salinity, pressure, temperature, and other quantities at spatial grid points. We do not access $x(\cdot)$ as functions, but only as a time-series $\mathbf{X}[n] = x(z[n])$ generated by evaluating $x(\cdot)$ along the otherwise-inaccessible state evolution $z[n]$. This means that at any time step n , vector $\mathbf{X}[n]$ contains $D = \#\text{variables} \times \#\text{gridpoints}$ values, so that the *snapshot matrix* \mathbf{X} representing an evolution over N timesteps is a $D \times N$ matrix \mathbf{X} .

The nature of the state space \mathcal{Z} is important only to the extent that it allows for a definition of the vector space of functions \mathcal{X} to which elements of $x(\cdot)$ belong. In applied contexts, this space is commonly taken to be the space $\mathcal{X} = L^p(\mathcal{Z}, m)$ of \mathbb{C} -valued functions, in particular with $p = 2$ where measure m is taken either to be a conserved measure of dynamics, or volume (Lebesgue measure) on \mathcal{Z} . Notice that this implies that $\dim \mathcal{X} \geq \dim \mathcal{Z}$.

The *Koopman operator* $\mathbb{K} : \mathcal{X} \rightarrow \mathcal{X}$ is the evolution rule advancing time for measurement functions $x \in \mathcal{X}$ by composing them with \mathbb{S}

$$\mathbb{K}x = x \circ \mathbb{S}, \quad (4)$$

or, evaluated pointwise,

$$\mathbb{K} \underbrace{x(z[n])}_{\mathbf{X}[n]} = x(\mathbb{S}(z[n])) = \underbrace{x(z[n+1])}_{\mathbf{X}[n+1]}. \quad (5)$$

Operator \mathbb{K} is analogous to \mathbb{S} for states z . Such evolution implies that $\mathbf{X}[n]$ at any point is determined by $\mathbf{X}[0]$:

$$\mathbf{X}[n] = \mathbb{K}\mathbf{X}[n-1] = \mathbb{K}^2\mathbf{X}[n-2] = \cdots = \mathbb{K}^n\mathbf{X}[0]. \quad (6)$$

Operator \mathbb{K} is linear, i.e., for any two functions x, \hat{x} and scalars a, b ,

$$\mathbb{K}(ax(\cdot) + b\hat{x}(\cdot)) = ax(\mathbb{S}(\cdot)) + b\hat{x}(\mathbb{S}(\cdot)) = a\mathbb{K}x + b\mathbb{K}\hat{x}. \quad (7)$$

Notice that this property holds regardless of \mathbb{S} being typically nonlinear. Effectively, the nonlinearity of \mathbb{S} on \mathcal{Z} is “unraveled” into additional dimensions of \mathcal{X} .

An eigenvalue $\mu \in \mathbb{C}$ and eigenfunction $\Psi : \mathcal{Z} \rightarrow \mathbb{C}$ (together: eigenpair) of \mathbb{K} satisfy

$$\mathbb{K}\Psi = \mu\Psi, \quad (8)$$

which implies that if $\Psi \in \mathcal{X}$ happens to be one of the measurement functions selected to form an element of $\mathbf{X}[n]$, its evolution $\Psi[n] = \Psi(z[n])$ would be given simply through multiplication by the associated eigenvalue

$$\Psi[n] = \mathbb{K}^n\Psi[0] = \mu^n\Psi[0]. \quad (9)$$

we can introduce *continuous-time eigenvalues*

$$\lambda = \rho + i\omega := \frac{1}{\Delta t} \ln \mu, \quad \text{or} \quad \mu = \exp(\lambda\Delta t) \quad (10)$$

so that the evolution $\mu^n = e^{\lambda n \Delta t}$ has an interpretation in terms of the original continuous time scale t both qualitatively and quantitatively.

To aid interpretation, we will for eigenvalues often note their period of oscillation P

$$P = 2\pi/\omega \quad (11)$$

and halving/doubling time τ

$$e^{\rho\tau} = 2, \quad \tau := \frac{\ln 2}{\rho} \quad (12)$$

which are expressed units of time. Interpretation as doubling vs. halving time is detected qualitatively from the sign of ρ or τ , positive for growing eigenfunctions and doubling time, negative for decaying eigenfunctions and halving time.

By linearity, if any measurement function x_p of the snapshot is a linear combination of eigenfunctions Ψ_k , $x_p(\cdot) = \sum_{k=0}^K \Phi_{pk} \Psi_k(\cdot)$ with coefficients $\Phi_{pk} \in \mathbb{C}$, $K \leq \infty$, then its time-trace would be given by

$$\mathbf{X}_p[n] = \mathbb{K}^n \left(\sum_{k=0}^K \Phi_{pk} \Psi_k \right) = \sum_{k=0}^K \Phi_{pk} \mu_k^n \underbrace{\Psi_k[0]}_{=:b_k} \quad (13)$$

Expanding *all* elements of vector-valued observation $x(\cdot)$ into the same set of eigenfunctions, gives rise to

$$\begin{bmatrix} | \\ \mathbf{X}[n] \\ | \end{bmatrix} = \sum_{k=0}^K \begin{bmatrix} | \\ \Phi_k \\ | \end{bmatrix} \mu_k^n b_k \quad \text{or} \quad \begin{bmatrix} | \\ \mathbf{X}(t) \\ | \end{bmatrix} = \sum_{k=0}^K \begin{bmatrix} | \\ \Phi_k \\ | \end{bmatrix} e^{t\lambda_k} b_k \quad (14)$$

where the two formulas are, respectively, continuous- and discrete-time versions of the decomposition, linked at timesteps $t = n\Delta t$. The column-vectors $\Phi_k \equiv \Phi_{*k} \in \mathbb{C}^D$ are called *Koopman modes*, and

We note here the similarity of the “separation-of-variables” in Koopman mode decomposition (KMD) (14) with the evolution employed by Empirical Orthogonal Functions (EOF) [4, 45], or Proper Orthogonal Decomposition (POD) [3]:

$$\mathbf{X}[n] = \underbrace{\sum_{k=0}^K \Phi_k b_k \mu_k^n}_{\text{KMD}} = \underbrace{\sum_{k=0}^K \mathbf{U}_k \sigma_k \mathbf{V}_k[n]}_{\text{EOF/POD}}. \quad (15)$$

While EOF/POD modes \mathbf{U}_k are real-valued and orthonormal, $\mathbf{U}_k^\top \mathbf{U}_{k'} = \delta_{kk'}$, Koopman modes are typically not orthonormal and appear in complex-conjugate pairs to capture oscillatory components. On the other hand, there is no *a priori* dynamics that can be assumed about temporal evolution of EOF/POD modes $\mathbf{V}_k[n]$, while Koopman mode evolution is easy to interpret, as it is always a decaying/growing/periodic evolution $\mu_k^n = e^{\rho_k n \Delta t} (\cos(\omega_k n \Delta t) \pm i \sin(\omega_k n \Delta t))$. Further discussion of the connections is available in [46, §4.3].

Dimension of a mode Φ_k is equal to the number of observables used to form $\mathbf{X}[n]$ because mode Φ_k stores the coefficients with which eigenfunction Ψ_k participates in evolution of snapshots $\mathbf{X}[n]$. Koopman modes correspond to spatial profiles that evolve in time according to a single time constant $\mu_k = e^{\Delta t \lambda_k}$.

When eigenvalues $\mu = e^\lambda$ are real-valued, the associated component of the decomposition (13) evolves as

$$\sim \Phi e^{\lambda t} b. \quad (16)$$

On the other hand, oscillating (complex-valued) modes appear in complex-conjugate pairs Φ, Φ_k^* that evolve according to eigenvalues μ, μ^* . The associated real-valued component of the decomposition (13) will be in the form

$$\begin{aligned} \sim \Phi^* e^{\rho t - i\omega t} b^* + \Phi e^{\rho t + i\omega t} b &= 2 \operatorname{Re}(\Phi e^{\rho t + i\omega t} b) \\ &= 2|\Phi|b|e^{\rho t} \cos(\omega t + \Theta + \theta) \end{aligned} \quad (17)$$

where the polar form of the mode and of the associated coefficient are

$$\Phi = |\Phi|e^{i\Theta}, \quad b = |b|e^{i\theta}. \quad (18)$$

Here $|\Phi|, \Theta$ are element-wise moduli and phases of Φ .

In summary, while both elements of the conjugate pair are needed for a *linear* decomposition (13), the formulation in terms of the magnitude and phase of the associated oscillation (17) is typically preferred for interpretation of the associated dynamics.

Returning to (14), the matrix form

$$\begin{bmatrix} | & & | & & | \\ \mathbf{X}[0] & \cdots & \mathbf{X}[n] & \cdots \\ | & & | & & | \end{bmatrix} = \underbrace{\begin{bmatrix} \cdots & | & \cdots \\ & \Phi_k & \\ & | & \end{bmatrix}}_{\Phi} \underbrace{\begin{bmatrix} \ddots & & \\ & b_k & \\ & & \ddots \end{bmatrix}}_{\operatorname{diag} b} \underbrace{\begin{bmatrix} \mu_k^0 & \cdots & \mu_k^n & \cdots \end{bmatrix}}_{\mu^\top} \quad (19)$$

clarifies that Koopman framework amounts to a formalism akin to solving a PDE by separation of variables, where the columns of the modal matrix Φ are *spatial profiles* constant in time, while rows of the μ^\top matrix are the *temporal time traces* according to which each of the modes evolves. The diagonal matrix $\operatorname{diag} b$ plays the role of the coefficients used to fit this spatiotemporal decomposition onto the first snapshot, as for the first $n = 0$ column this reduces to

$$\mathbf{X}[0] = \Phi \begin{bmatrix} \ddots & & \\ & b_k & \\ & & \ddots \end{bmatrix} \begin{bmatrix} 1 \\ \vdots \end{bmatrix} = \Phi b. \quad (20)$$

Remembering that b is derived from eigenfunctions of the Koopman operator (13) and the initial condition of the evolution $z(0)$, we realized that the eigenfunctions and initial conditions are entangled in a vector of coefficients $\Psi[0] = \Psi(z(0))$ formed by evaluations of all eigenfunctions at the initial condition of the evolution. Theoretically, dimension of Ψ is infinite, although rank of the input data matrix \mathbf{X} limits the number of eigenfunctions that are practically accessible.

3.2. Dynamic Mode Decomposition as numerical Koopman analysis

Dynamical Mode Decomposition (DMD) [1, 2] is the algorithm that is able to approximate the decomposition (13) in a non-parametric manner, i.e., without *a priori* specifying

the location of eigenvalues. While the derivation of this algorithm is not new [46], we repeat it here because it clarifies how the choice of parameters affects the outcome, and allows us to comment on modifications we performed in Section 3.3.

Starting with the snapshot matrix $\mathbf{X} = \mathbf{X}[n]$, $n = 0, 1, \dots, N - 1$, subdivide it into a “past” and “future”:

$$\begin{aligned}\mathbf{X}_1 &= [\mathbf{X}[0] \quad \mathbf{X}[1] \quad \dots \quad \mathbf{X}[N - 2] \quad \dots] \in \mathbb{R}^{m \times (N-1)} \\ \mathbf{X}_2 &= [\mathbf{X}[1] \quad \dots \quad \mathbf{X}[N - 2] \quad \mathbf{X}[N - 1]] \in \mathbb{R}^{m \times (N-1)}\end{aligned}\quad (21)$$

While evolution $\mathbf{X}(z[n]) \mapsto \mathbf{X}(z[n + 1]) = \mathbf{K}\mathbf{X}(z[n])$ is connected by the infinite-dimensional Koopman operator, we approximate it using left-multiplication by the DMD matrix \mathbf{K}

$$\mathbf{X}[n + 1] = \mathbf{K}\mathbf{X}[n], \quad (22)$$

or

$$\mathbf{X}_2 = \mathbf{K}\mathbf{X}_1. \quad (23)$$

This amounts to the assumption that $\mathbf{X}[n]$ were generated as iterations of a finite-dimensional linear map.

Further assuming that this map has a complete set of eigenvectors Φ_m with eigenvalues $\mu_m \in \mathbb{C}$, which is the generic case under small random perturbations of matrix elements, we write

$$\mathbf{X}[n] = \sum_{m=1}^M \Phi_m b_m \mu_m^n, \quad (24)$$

where coefficients b_m are determined by the initial condition

$$\mathbf{X}[0] = \sum_{m=1}^M \Phi_m b_m = \Phi b. \quad (25)$$

To make the choice of coefficients unique, we normalize each Φ_m to $\|\Phi_m\| = 1$. We refer to Φ_m as *DMD modes*, to μ_m as *DMD eigenvalues*, and to b_m as *reconstruction coefficients*. Magnitudes $|b_m|$ are norms of DMD modes.

Of course, this decomposition of dynamics exactly mirrors (14), so the common thread for all DMD algorithms is computation of eigenvalues and eigenvectors of \mathbf{K} . Equation (23) can be solved approximately by finding the ℓ^2 -optimal solution that minimizes the Frobenius norm

$$\mathbf{K} := \arg \min_{\mathbf{A}} \|\mathbf{A}\mathbf{X}_1 - \mathbf{X}_2\|_F. \quad (26)$$

When the number of time-steps is smaller than the dimension of a snapshot, making \mathbf{X} a “tall” matrix, this is equivalent to forming the Moore–Penrose pseudoinverse \mathbf{X}_1^\dagger and setting

$$\mathbf{K} = \mathbf{X}_2 \mathbf{X}_1^\dagger \quad (27)$$

which amounts to

$$\mathbf{K} = \mathbb{K} \mathbf{U} \mathbf{U}^\top, \quad (28)$$

where \mathbf{U} is the orthonormal basis for the data subspace $\text{span}\{\mathbf{X}[n]\}_{n=0}^{N-2}$, so that $\mathbf{U} \mathbf{U}^\top$ is the orthogonal projector onto the subspace spanned by first $N - 1$ snapshots.

This route is often impractical. Storing the square matrix \mathbf{K} requires m^2 values, even though we are practically interested in some small subset of vectors (DMD modes), each of length m . Moreover, operations involving this matrix are known to be numerically-fragile [47], so an alternative route is needed. Finally, solving (25) for coefficients b again requires for a fitting, which can be performed either in the same or different norm/process as fitting of \mathbf{K} . Various flavors of the DMD algorithm available in the literature differ in the choices they make to address these questions (among their other differences).

Here we present the simplest version, the so-called “exact” DMD [46]. In it, the fitting of \mathbf{K} is made in the ℓ^2 -space of matrices, using the Singular Value Decomposition. The dimensionality of \mathbf{K} is resolved by first projecting dynamics to a lower-dimensional subspace of r singular vectors \mathbf{U}_r of \mathbf{X}_1 , and then (implicitly) choosing a non-orthogonal basis of DMD modes in that subspace, to recover the requirement that each mode corresponds to a single (complex) time constant (10). Finally, the fitting of b is again performed in ℓ^2 -space of vectors. We point out that the process below does not completely resolve the issue of numerical robustness; for details see [48, 49].

First, we compute the truncated singular value decomposition of \mathbf{X}_1

$$\mathbf{X}_1 \approx \mathbf{U}_r \boldsymbol{\Sigma}_r \mathbf{V}_r^\top \quad (29)$$

where $\mathbf{U}_r \in \mathbb{R}^{m \times r}$, $\mathbf{V}_r \in \mathbb{R}^{(N-1) \times r}$, $\boldsymbol{\Sigma}_r \in \mathbb{R}^{r \times r}$ are matrices of first r left- and right-singular vectors and singular values, respectively.

Equation (23) then becomes

$$\mathbf{X}_2 \approx \mathbf{K} \mathbf{U}_r \boldsymbol{\Sigma}_r \mathbf{V}_r^\top, \quad (30)$$

and therefore,

$$\tilde{\mathbf{K}} := \mathbf{U}_r^\top \mathbf{K} \mathbf{U}_r = \mathbf{U}_r^\top \mathbf{X}_2 \mathbf{V}_r \boldsymbol{\Sigma}_r^{-1}. \quad (31)$$

Since \mathbf{U}_r is a subset of columns of \mathbf{U} , this implies that

$$\tilde{\mathbf{K}} = \mathbf{U}_r^\top \mathbb{K} \mathbf{U}_r \quad (32)$$

so that eigenvalues of $\tilde{\mathbf{K}}$ are a subset of eigenvalues of \mathbf{K} and \mathbb{K} .

The Eigendecomposition

$$\tilde{\mathbf{K}} \tilde{\Phi}_k = \mu_k \tilde{\Phi} \quad (33)$$

gives a good approximation of Koopman eigenvalues, but $\tilde{\Phi}$ are still only r -dimensional.

Merely “undoing” the compression by \mathbf{U}_r and setting $\Phi \approx \Phi'_k := \mathbf{U}_r \tilde{\Phi}$ produces eigenvectors that have the correct number of elements, but are constrained to be in the artificially-reduced span \mathbf{U}_r :

$$\mathbf{U}_r \mathbf{U}_r^\top \mathbf{K} \underbrace{\mathbf{U}_r \tilde{\Phi}_k}_{\Phi'_k} = \mu_k \underbrace{\mathbf{U}_r \tilde{\Phi}}_{\Phi'_k}. \quad (34)$$

Matrix $\mathbf{U}_r \mathbf{U}_r^\top \mathbf{K}$ is the DMD matrix whose output is projected onto the lower-dimensional subspace. Such calculation may be favorable in cases where the size of the input data set prohibits computing more than r largest singular vectors [50], but if the full SVD decomposition is available, *exact* DMD can do better. From SVD $\mathbf{X}_1 = \mathbf{U} \mathbf{\Sigma} \mathbf{V}^\top$, where number of columns of \mathbf{U} and \mathbf{V} is equal to rank \mathbf{X}_1 , the exact DMD prescription makes use of it by setting

$$\Phi_k := \mathbf{X}_2 \mathbf{V} \mathbf{\Sigma}^{-1} \tilde{\Phi}_k. \quad (35)$$

To calculate combination vector b , one solves the initial condition equation (25) by ℓ^2 -minimization

$$\mathbf{X}[0] = \Phi b \rightarrow b = \Phi^\dagger \mathbf{X}[0], \quad (36)$$

which then ensures that the data $\mathbf{X}[0]$ is well-approximated (in the ℓ^2 sense)

$$\mathbf{X}[n] \approx \sum_k \Phi_k \mu_k^n b_k = \sum_k \Phi_k e^{\lambda_k n \Delta t} b_k. \quad (37)$$

The full process is summarized in Algorithm 1.

DMD eigenvalues and modes are not canonically ordered by importance; this is in contrast to POD/EOF modes which are typically ordered by the magnitude of the associated singular value. Therefore, ordering and selection of DMD modes is an additional step that is typically performed by taking account of the purpose that the DMD computation serves in the overall modeling process. Since the mode selection is less standard than mode computation, as it may be specific to the model analyzed, we address it in a separate section.

3.3. Improving interpretability, stability, and robustness

For the purposes of this paper, we report on DMD analysis of the three-dimensional velocity fields. This suggests that each snapshot in \mathbf{X} contains three velocity components $[u, v, w]$ evaluated on the spatial grid. We augment this variable vector by the horizontal speed and use

$$\frac{\sqrt{2}}{2} \begin{bmatrix} U_x \\ U_y \\ \sqrt{2}U_z \\ \sqrt{U_x^2 + U_y^2} \end{bmatrix} \quad (38)$$

as the snapshot vector. Since the horizontal speed $U_s := \sqrt{U_x^2 + U_y^2}$ is a nonlinear function of U_x, U_y , computing its DMD decomposition from knowing only decomposition of U_x, U_y

Algorithm 1: Exact DMD algorithm. For details see Section 3.2.

```

input : Data matrix  $\mathbf{X}$ , with columns  $\mathbf{X}[k], n = 0, \dots, N - 1$ 
input : Snapshot sampling rate  $\Delta t$ 
input : Dimension of the subspace  $r$ 

 $\mathbf{X}_1 \leftarrow \mathbf{X}[0], \dots, \mathbf{X}[N - 2], \quad \mathbf{X}_2 \leftarrow \mathbf{X}[1], \dots, \mathbf{X}[N - 1]$ 
 $U, \Sigma, V \leftarrow \text{svd}(\mathbf{X}_1)$  // Singular Value Decomposition
 $\mathbf{U}_r \leftarrow \mathbf{U}[1 : r, :], \Sigma_r \leftarrow \Sigma[1 : r, 1 : r], \mathbf{V}_r \leftarrow \mathbf{V}[1 : r, :]$  // Reduce to  $r$ -dim.
    subspace
 $\tilde{\mathbf{K}} \leftarrow \mathbf{U}_r^\top \mathbf{X}_2 \mathbf{V}_r \Sigma_r^{-1}$  // DMD matrix
 $\mu_k, \tilde{\Phi}_k \leftarrow \text{eig}(\tilde{\mathbf{K}})$  // Eigendecomposition
 $\Phi_k \leftarrow \mathbf{X}_2 \mathbf{V} \Sigma^{-1} \tilde{\Phi}_k$  // Koopman modes
 $\Phi_k \leftarrow \Phi_k / \|\Phi_k\|_2$  // Mode normalization
 $\lambda_k \leftarrow (\ln \mu_k) / \Delta t$  // Continuous-time DMD eigenvalues
 $b \leftarrow \Phi_k^\top \mathbf{X}[0]$  //  $\ell^2$  fit of the 1st snapshot
output:  $\Phi_k, \lambda_k, b_k$ 

```

would require combining all available DMD modes, complicating any model reduction. Including the horizontal speed as an explicit observable avoids doing so. The $\sqrt{2}$ factors ensure that the ℓ^2 norm of any snapshot approximates the integrated ℓ^2 -norm of the three-dimensional velocity field, avoiding biasing of any component. Our simulated data has 144 snapshots, amounting to a 6d window sampled at 1h. The size of the computational grid is $190 \times 96 \times 32$; evaluating the four observables on it and stacking as in (38) yields the snapshot matrix of dimensions $2,334,720 \times 144$.

Several articles have argued for and against removing the mean value of data as the first pre-processing step [51–53]. If the trajectory is long and the dynamics stationary, in the sense that the spectrum does not change over time, computing the mean

$$\Phi_0 := \frac{1}{N} \sum_{n=1}^N \mathbf{X}[n] \quad (39)$$

and subtracting it from data amounts to orthogonally-projecting the data onto the $\lambda = 1$ eigenfunction of the Koopman operator [8]. This can be thought of as a “parametric” estimation of the Koopman mode, as we presume to know *a priori* the eigenvalue $\lambda = 1$ of interest. However, when the duration of data is short and the dynamics possesses eigenvalues off the unit circle, the practical utility of mean-removal and theoretical implications were less understood. Recent investigations suggest that mean-removal increases the robustness of the algorithm without compromising the integrity of the analysis [52, 53]. We have evaluated the outcomes of the algorithm with and without the mean removal and concluded that the approximation quality of non-constant modes is improved in the case where no mean removal is performed. The likely cause is the lack of orthogonality of DMD modes. Since

the data mean vector is recurrent with respect to any period P , removing it parametrically as above removes a degree of freedom in subsequent estimation of periodic modes and regression of data on them. The same problem does not occur in POD/EOF reduced order models, since the constraint of orthogonality of modes prevents the data mean to contribute to any other mode except the “mean mode”.

As detailed in [54, 55], the baseline DMD algorithm suffers from bias in eigenvalues due to using only \mathbf{X}_1 (past snapshots) to construct the lower-dimensional subspace, amounting to the least-squares (LSQ) regression of the subspace onto the data. Instead, we use the total-least-squares (TLSQ) correction [55] by projecting $\mathbf{X}_1, \mathbf{X}_2$ matrices onto a subspace derived from the SVD of a larger \mathbf{Z} matrix, formed by vertically stacking $\mathbf{X}_{1,2}$ matrices. Conceptually, this step is simple to implement, although the SVD of the matrix \mathbf{Z} now requires twice as much memory as before.

We adopt the following additional modifications of the baseline exact DMD based on [49].

- (a) Columns of matrices $\mathbf{X}_1, \mathbf{X}_2$ are normalized by ℓ^2 -norms of matrix \mathbf{X}_1 , improving the condition number and therefore making numerical algebra more robust [49, §3.4].
- (b) In our implementation of DMD we replaced MATLAB’s stock divide-and-conquer SVD algorithm with the LAPACK QR SVD algorithm which computes the small singular values and the associated singular vectors to a higher accuracy [49, §4.1.3].
- (c) We evaluated the RRR modification to DMD [49, §3.5], which optimizes the residual of eigenvector equation for $\tilde{\mathbf{K}}$ for the DMD eigenvalues and eigenvectors. The changes compared to the baseline exact DMD algorithm were minimal; to avoid a substantial computational cost we did not use the RRR modification here.

The baseline DMD algorithm Algorithm 1 computes b by minimizing the fit of the DMD model at the initial condition over all complex-valued vectors v , $b = \arg \min_v \|\Phi v - \mathbf{X}[0]\|_2^2$. Since eigenvalues are already known at that point in the algorithm, in principle any other snapshot, $n' \neq 0$, could have been chosen for the optimization target as in

$$\arg \min_v \left\| \Phi \operatorname{diag} \begin{bmatrix} \mu_1^{n'} & \mu_2^{n'} & \dots \end{bmatrix} v - \mathbf{X}[n'] \right\|_2^2.$$

Practically, the size of coefficients b will slightly change depending on the choice of the time step. Since all modes were normalized to the unit ℓ^2 norm, any decaying modes will be assigned relatively higher coefficients when $n' = 0$ is chosen while the growing modes will be assigned relatively higher coefficients when $n' \gg 0$. For steady-state data, we should expect that the relative importance of modes does not change, therefore we can choose b that minimizes the total error across all snapshots

$$b = \arg \min_v \sum_{n=0}^{N-1} \left\| \mathbf{X}[n] - \Phi \operatorname{diag} \begin{bmatrix} \mu_1^n & \mu_2^n & \dots \end{bmatrix} v \right\|_2^2. \quad (40)$$

This equation can be converted to a plain algebraic linear system through the use of a tensor product of eigenmode and eigenvalue matrices. Solving (40) for all $n = 0, 1, \dots, N - 1$ on

a computer can require a substantial amount of working memory so, instead, we use only a small subset of snapshots spread over the entire time domain to ensure minimal biasing of growing/decaying modes, while keeping computation cost at bay.

Algorithm 2: Modified exact DMD algorithm.

```

input : Data matrix  $\mathbf{X}$ , with columns  $\mathbf{X}[k], n = 0, \dots, N - 1$ 
input : Snapshot sampling rate  $\Delta t$ 
input : Dimension of the subspace  $r$ 

 $\mathbf{X}_1 \leftarrow \mathbf{X}[0], \dots, \mathbf{X}[N - 2], \quad \mathbf{X}_2 \leftarrow \mathbf{X}[1], \dots, \mathbf{X}[N - 1]$ 
 $\mathbf{X}_1[:, k] \leftarrow \mathbf{X}_1[:, k] / \|\mathbf{X}_1[:, k]\|_2, \quad \mathbf{X}_2[:, k] \leftarrow \mathbf{X}_2[:, k] / \|\mathbf{X}_1[:, k]\|_2$ 
    // Normalization
 $\mathbf{Z} \leftarrow [\mathbf{X}_1; \mathbf{X}_2]$                                 // TLSQ start
 $\mathbf{U}_Z, \Sigma_Z, \mathbf{V}_Z = \text{QRsvd}(\mathbf{Z}), \mathbf{V}_{Z,r} \leftarrow \mathbf{V}_Z[1:r, :]$       // using QR-based SVD
 $\mathbf{X}_1 \leftarrow \mathbf{X}_1 \mathbf{V}_{Z,r}, \quad \mathbf{X}_2 \leftarrow \mathbf{X}_2 \mathbf{V}_{Z,r}$           // TLSQ projection
 $\mathbf{U}, \Sigma, \mathbf{V} \leftarrow \text{QRsvd}(\mathbf{X}_1)$                                 // QR-based SVD
 $\mathbf{U}_r \leftarrow \mathbf{U}[1:r, :], \Sigma_r \leftarrow \Sigma[1:r, 1:r], \mathbf{V}_r \leftarrow \mathbf{V}[1:r, :]$  // Reduce to  $r$ -dim.
    subspace
 $\tilde{\mathbf{K}} \leftarrow \mathbf{U}_r^\top \mathbf{X}_2 \mathbf{V}_r \Sigma_r^{-1}$                                 // DMD matrix
 $\mu_k, \tilde{\Phi}_k \leftarrow \text{eig}(\tilde{\mathbf{K}})$                                 // Eigendecomposition
 $\Phi_k \leftarrow \mathbf{X}_2 \mathbf{V} \Sigma^{-1} \tilde{\Phi}_k$           // Koopman modes
 $\Phi_k \leftarrow \Phi_k / \|\Phi_k\|_2$                                 // Mode normalization
 $\lambda_k \leftarrow (\ln \mu_k) / \Delta t$           // Continuous-time DMD eigenvalues
 $b \leftarrow \arg \min_v \sum_{n \in [0, N-1]} \left\| \mathbf{X}[n] - \Phi \text{diag} \begin{bmatrix} \mu_1^n & \mu_2^n & \dots \end{bmatrix} v \right\|_2^2$  //  $\ell^2$  fit
output:  $\Phi_k, \mu_k, \lambda_k, b_k$ 

```

4. Analysis of the DMD spectrum and DMD modes

The number of linearly independent modes that can be calculated from the full snapshot \mathbf{X} is its rank, which in our case is capped by the number of snapshots $N = 144$. We now further want to extract a smaller number of modes in order to investigate them more deeply and to build a low-rank representation of data.

4.1. SVD subspace selection

The first step in model reduction of DMD is the choice of parameter r which restricts the snapshot matrices $\mathbf{X}_1, \mathbf{X}_2$ to the r -dimensional subspace spanned by singular vectors of \mathbf{X}_1 . Projections of \mathbf{X}_1 onto such subspaces amount to ℓ^2 -norm optimal approximations of \mathbf{X}_1 by r -ranked matrices (Eckart–Young theorem). Since all subsequent calculations will be restricted to that subspace, the choice of r can dramatically affect the outcome of DMD. There are no universal guidelines for choosing r . If the choice of r is analyzed

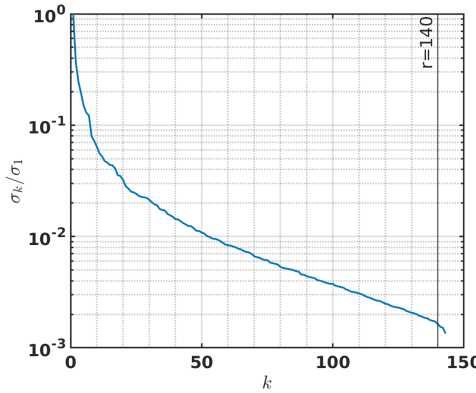


Figure 8: Singular values of the data matrix do not show significant separations of scale beyond the initial modes. The vertical line indicates the truncation value employed in our analysis.

separately from the DMD context in which we use it, then [56] provides a threshold that removes iid, zero-mean additive noise, [57] reviews several different analytic and heuristic recipes for choosing the cutoff, while [49] uses the numerical rank of the matrix (number of normalized singular values larger than a chosen threshold). We remain agnostic with respect to the specific choice, and note that the dominant DMD modes are computed robustly as long as r is chosen away from the extreme values, for the following reasons.

Choosing r too small limits the number of linearly independent DMD modes that can be computed; typically, r should not be made smaller than the number of physically-relevant DMD modes, if there is prior information about them. However, even if there is intuition about the physically-relevant modes, they may not be dominant in the ℓ^2 sense. For this reason, one should choose r larger than expected, and perform the mode selection after all r DMD modes have been computed.

Choosing r too large can include into the subspace directions that are associated with noise (numerical or otherwise) into the computation. DMD computations can be fragile with respect to the level of added noise, so it is prudent to remove at least some of the singular values in the tail.

For the remainder of the paper, we chose $r = 140$ as the cut off. The singular values spectrum in Figure 8 does not show particular spectral gaps, or leveling off, that may be associated with the presence of noise. We have tested several additional choices of values r between 80 and 143 (the rank of the data matrix and number snapshots) without noticeable impact on the quality of the remainder of the analysis.

4.2. Robustness of eigenvalues

Algorithm 2 serves to efficiently estimate eigenvalues and eigenvectors of the matrix \mathbf{K} by effectively performing a linear regression on pairs of snapshots

$$\mathbf{K} := \arg \min_A \|\mathbf{X}_2 - A\mathbf{X}_1\|. \quad (41)$$

If the number of snapshots is large, omitting a pair of snapshots would not distort resulting eigenvalues. However, with a finite number of snapshots, the DMD eigenvalues do change slightly, but noticeably, even if a single snapshot is omitted. When the expected frequencies of modes are well-separated, this likely does not pose a problem. However, in the case of the analyzed data, periods of diurnal and semidiurnal tidal components used to force the model are tightly clustered around 12h and 24h, differing sometimes only in third or forth significant digit. Consequently, the resulting small uncertainty in eigenvalues prevent us from clearly identifying a single DMD mode with a single tidal pattern.

To estimate the robustness of the linear regression with respect to the amount of data given, we perform the leave-one-out analysis. After computing the DMD eigenvalues and modes for the full data set, we repeat the computation of eigenvalues 30 times while erasing at random i th columns $\mathbf{X}_1[:, i], \mathbf{X}_2[:, i]$ from the pair of matrices.

The resulting collection of eigenvalue spectra is used in a Kernel Density Estimates (KDE) of the distribution of eigenvalues. A set of $30 \times r$ eigenvalues $\hat{\mu}_i$, where $r = 140$ is the dimension of the SVD subspace, is converted to a continuous density on the complex plane $z \in \mathbb{C}$ via

$$d_h(z) \propto \sum_k \exp \frac{-|z - \hat{\mu}_k|^2}{h^2}, \quad (42)$$

where h is the bandwidth parameter that controls the width of each Gaussian superimposed at locations of eigenvalues, and the density is normalized to unit mass. Choosing h wider or narrower produces a smoother or more localized density estimate. Eigenvalues that do not move significantly between leave-one-out experiments result produce density that is concentrated over small subsets of complex plane, while high-variability eigenvalues result in a smeared-out parts of the density.

In Figure 9, eigenvalues aggregate in well-defined clusters around frequencies associated with tidal components used to force the model (Table 2). An exception is the robust cluster around $P \approx 5h$ which is not a harmonic of any input frequency. As expected, shorter time periods, where only a few snapshots are available per period, are less robustly computed. Eigenvalues close to the unit circle, e.g., as seen in panel Figure 9(d) will commonly result in leave-one-out perturbations that straddle the unit circle, that is result in slightly growing or slightly decaying modes; this analysis shows that such behavior can be the result of finite-length data set, rather than physical growth or decay.

In addition to visualization, the density $d_h(z)$ estimated from leave-one-out eigenvalues $\hat{\mu}_k$ can be evaluated at locations of eigenvalues μ_n computed for the full set of snapshots.

The values $d_h(\mu_n)$ provide an estimate of robustness of eigenvalues μ_n to perturbations in available data; they are reported in the summary Table 3.

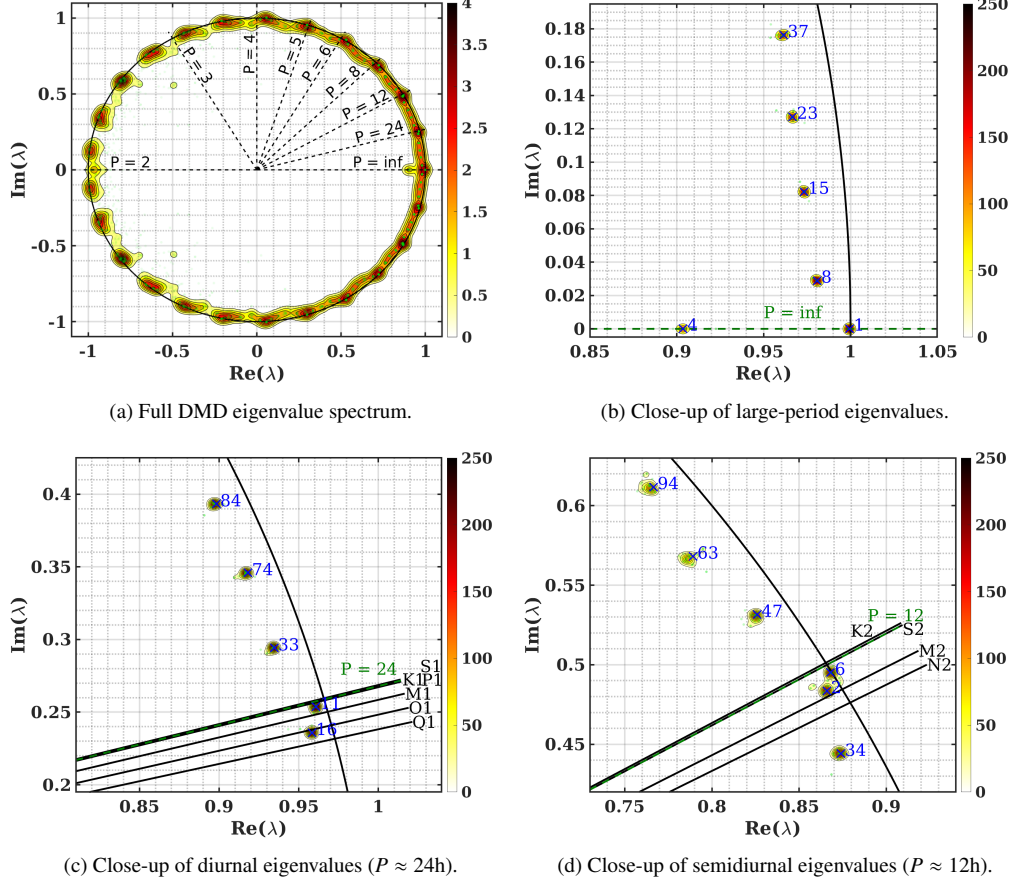


Figure 9: The spectrum of DMD discrete-time eigenvalues μ_k . Unit circle separates decaying modes (inside) from growing modes (outside). Diagonal lines indicate frequencies corresponding to tidal components used in forcing (Table 2). Colored contours show Gaussian kernel density estimates (KDE) based on leave-one-out analysis. Kernel bandwidth is $h = 2.5 \times 10^{-2}$ in panel (a) and $h = 2.0 \times 10^{-3}$ in zoomed-in panels (b)–(d). Blue crosses indicate eigenvalues computed using all the snapshots with numbers corresponding to the RMS rank of each mode as reported in Table 3.

4.3. Contributions of individual modes

There is no *a priori* ranking of DMD modes that can be used to easily define a criterion for the ranking of modes by their “importance”. The ℓ^2 norm of each mode, $|b_k|$, is one natural model-agnostic candidate, but decay rates (to identify persistent modes), ℓ^2 contributions to a subset of physical variables, or other characterizations of modes (see [58]) may

Index	Cluster	Period	Halving (−)/ Doubling (+) Time	RMS \tilde{b}_n	${}_w\tilde{b}_n$	Robustness $d_h(\lambda_n)$	Index	Cluster	Period	Halving (−)/ Doubling (+) Time	RMS \tilde{b}_n	${}_w\tilde{b}_n$	Robustness $d_h(\lambda_n)$
1	1	Inf	−1078.97	157.02	0.74	282.78	67	4	8.56	−44.77	4.83	0.14	141.89
2	3	12.34	−84.48	75.46	1.05	181.47	70	10	2.72	−25.92	4.65	0.24	5.55
4	1	Inf	−6.84	74.58	1.58	163.53	71	7	3.94	−15.78	4.49	0.19	3.78
6	3	12.12	−1029.16	69.55	0.94	190.64	74	2	17.44	−36.43	4.43	0.08	179.05
8	1	212.95	−36.32	56.86	0.52	257.16	76	7	4.06	−141.09	4.11	0.14	35.12
10	NaN	2.80	−3.26	36.87	2.00	0.00	78	5	5.70	−27.64	3.79	0.12	15.80
11	2	24.34	−112.00	33.99	0.37	236.18	80	7	4.54	−18.55	3.78	0.17	6.04
13	13	2.00	−3.59	27.67	1.63	0.00	82	8	3.47	−38.53	3.66	0.17	10.31
15	1	74.50	−29.33	25.15	0.24	230.53	84	2	15.22	−35.50	3.49	0.07	184.71
16	2	26.04	−53.05	19.28	0.32	217.63	85	9	3.07	−107.53	3.30	0.14	10.21
19	10	2.81	−7.39	16.41	0.89	0.00	88	8	3.53	+212.17	3.05	0.14	122.36
21	13	2.14	−4.58	16.29	0.93	0.01	90	5	6.69	−24.35	2.81	0.10	41.60
23	1	48.02	−27.34	15.04	0.18	197.61	92	9	3.11	−249.05	2.70	0.12	32.26
24	5	6.19	+90.93	11.11	0.22	199.52	94	3	9.33	−35.46	2.44	0.07	99.96
26	11	2.57	−7.01	10.77	0.58	0.00	95	12	2.23	−49.59	2.38	0.14	13.64
28	9	2.97	−8.75	9.75	0.50	2.92	98	10	2.75	+6512.72	2.27	0.12	49.60
30	4	8.26	−2531.05	9.29	0.20	210.09	100	11	2.47	−557.29	1.99	0.10	18.20
33	2	20.60	−34.22	8.85	0.15	212.79	101	8	3.68	−21.23	1.87	0.10	0.31
34	3	13.36	−34.92	8.84	0.17	186.66	104	8	3.60	−47.45	1.57	0.08	22.00
37	1	34.67	−30.36	8.51	0.13	188.51	106	7	4.38	−31.32	1.55	0.08	4.40
39	6	4.95	−36.89	8.20	0.33	37.57	107	6	5.13	−48.67	1.52	0.06	65.01
41	12	2.29	−8.28	7.60	0.44	0.00	109	8	3.75	−35.62	1.42	0.08	3.94
43	6	4.95	−943.33	7.44	0.25	130.84	111	7	4.23	−50.03	1.38	0.06	37.96
45	4	7.92	−47.62	6.99	0.19	102.78	114	6	5.41	−41.12	1.36	0.05	19.34
47	3	10.99	−38.63	6.56	0.14	157.12	116	11	2.51	−58.72	1.32	0.07	0.02
49	4	7.43	−22.31	6.14	0.21	33.50	117	12	2.26	−1149.21	1.13	0.07	38.18
50	12	2.38	−10.92	6.05	0.36	4.73	120	9	3.16	−103.37	1.07	0.06	55.52
53	5	5.97	−73.14	5.83	0.15	65.46	121	9	3.21	−66.38	1.06	0.06	2.77
55	5	6.99	−18.17	5.41	0.20	19.44	123	13	2.06	−614.10	0.94	0.05	31.39
56	7	4.15	+140.13	5.11	0.16	107.07	125	11	2.42	−20.55	0.89	0.06	0.00
58	9	3.32	−10.05	5.08	0.26	2.27	128	13	2.11	−386.21	0.83	0.05	1.20
60	5	6.34	−52.22	5.02	0.14	107.70	129	11	2.53	−102.69	0.79	0.05	27.99
63	3	10.07	−24.71	4.97	0.13	62.55	132	12	2.30	−2059.91	0.75	0.05	60.64
65	6	4.75	−35.73	4.90	0.19	12.03	133	13	2.09	−251.43	0.72	0.05	1.12
66	13	2.00	−13.31	4.88	0.30	8.35	136	13	2.14	−21.67	0.67	0.05	2.09
67	4	8.56	−44.77	4.83	0.14	141.89	138	10	2.78	−28.79	0.64	0.04	0.00
							139	10	2.81	−124.00	0.51	0.03	38.63

Table 3: Properties of DMD modes. Only one conjugate is listed for each complex mode pair. Robustness is estimated using kernel width $h = 2 \times 10^{-3}$. Clusters were assigned based on level sets of kernel density estimates with $h = 2.5 \times 10^{-2}$; label “NaN” indicates modes that do not belong to a well-defined cluster.

be equally or even more important depending on the model analyzed using DMD. We here showcase several such possibilities in the context of ocean dynamics.

Magnitudes of coefficients $|b_k|$ used to assemble the model of the evolution reflect how much each mode contributes to the initial condition (25). Unfortunately, such comparison will favor modes that are decaying, as their magnitude is initially large and then decreases in time.

To account for this, we calculate the Root Mean Square (RMS) norm of each mode over time

$$\tilde{b}_i^2 = \frac{1}{T} \int_0^T \|b_i e^{\lambda_i t} \Phi_i\|^2 dt = |b_i|^2 \frac{e^{2\rho_i T} - 1}{2\rho_i T} \quad (43)$$

$$\tilde{b}_i = |b_i| (1 + \rho_i T/2 + \dots), \quad (44)$$

where $\rho_i = \operatorname{Re} \lambda_i$. The expansion demonstrates that the correction will reduce the signifi-

cance of decaying ($\rho_i < 0$) modes and boost the significance of growing modes, but only when $|\rho_i T|$ is close to 1 or larger.

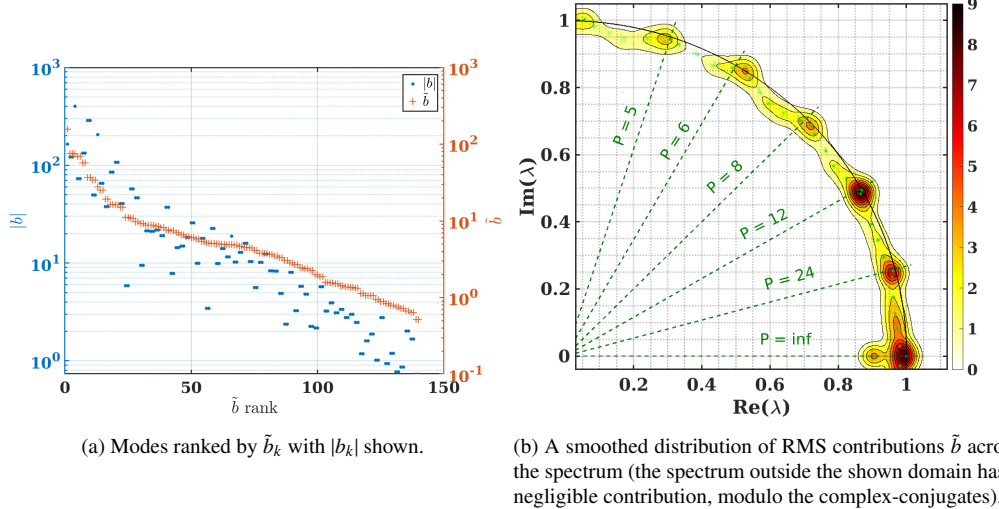


Figure 10: The distribution of RMS \tilde{b}_k across the eigenvalue spectrum and comparison with $|b_k|$.

Figure 10 shows the difference in ranking the modes using mode contributions to the initial condition b vs. RMS contributions of modes. Majority of modes would be similarly ranked toward the beginning or end of the spread regardless of the choice, but for some the difference is significant. For purposes of visualization, the concentration of RMS contributions across the spectrum of DMD eigenvalues is represented by the heat map of kernel density estimate of eigenvalues in Figure 10b. Each eigenvalue has been weighted by its RMS coefficient \tilde{b} to yield the function

$$\tilde{b}(z) := \sum_{k=1}^r \tilde{b}_k \exp \frac{-|z - \mu_k|^2}{h^2}, \quad (45)$$

where kernel bandwidth $h = 2 \times 10^{-3}$ was chosen. It is clear that semidiurnal and diurnal eigenvalues dominate in terms of RMS contribution, followed by long-period and terdiurnal ($P \approx 8\text{hour}$) eigenvalues. Notice also the $P \approx 5\text{hour}$ group of modes which does not correspond to either principal tides or their harmonics (“overtides”).

Model-agnostic methods of ranking the modes, such as norm-contributions b_k, \tilde{b}_k would in practice be supplemented by model-specific considerations. For example, in the particular case of tides one could keep harmonics of fundamental tides (“overtides”) as the part of the model, even when their RMS is not very high. Similar discussions along these lines for EOF/POD modeling can be found in [45, 59, 60]. An example of discrimination based on the decay rates is shown by the distinction between left and right panels in Figure 11

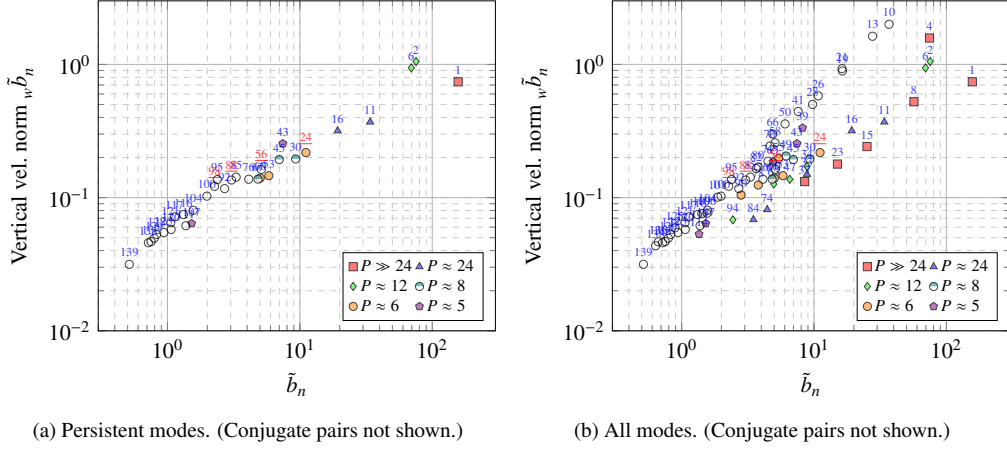


Figure 11: Comparison between RMS of the total and the vertical velocity norms of modes. Indexes of modes correspond to Table 3; marker shapes are used to indicate memberships in primary clusters of interest classified according to their oscillation periods P ; underlined labels correspond to growing modes. Left panel omits *non-persistent* modes (46).

and Figure 12 where modes are deemed non-persistent if their initial magnitude decays to less than 10% of the initial magnitude, i.e., if

$$e^{\rho T} < 0.1, \text{ for } T = 143\text{hour} \quad (46)$$

which translates into half-life times

$$-43 < T_{1/2} < 0. \quad (47)$$

One purpose of such selection of variables would be to discard the initial transient, for example, in simulations that are not initialized on the attractor of dynamics.

The vertical velocity in the simulated ocean is by, roughly, two orders of magnitude smaller than the total velocity; therefore comparing modes by total velocity potentially obscures how the vertical transport is distributed across the modes. To evaluate what modes are important for the vertical transport we additionally calculate the ℓ^2 norm of mode elements corresponding to vertical velocities ${}_w b_k$, and the associated RMS contribution ${}_w \tilde{b}_k$, analogously to (43). Figure 11 shows that the magnitudes of total and vertical velocities correlate. In both cases, the correlation roughly linear, indicating that the modes with strongest vertical activity in most cases rank highly in terms of the norm of the full velocity field. Further exploration of the correlations is beyond the scope of this paper.

Finally, Figure 12 demonstrates correlations between robustness of eigenvalues, as estimated by $d_h(\lambda_k)$ estimate (42), and the contributions, as measured by b_k or \tilde{b}_k . The robust, high-contributing modes would be located in the upper right corner of each of the graphs, and are the top candidates for building any low-rank model of the data. Modes that score well on one, but not both axes are in top left, and bottom right, and depending on the purpose of a low-rank model, one or both of these groups could be included. Modes close to

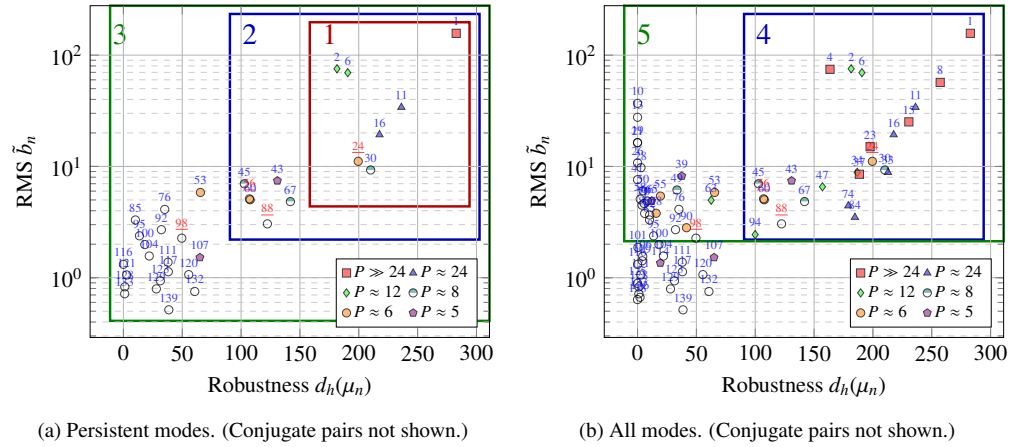


Figure 12: Arrangement of DMD modes with respect to RMS \tilde{b}_k and robustness $d_h(\mu_k)$ with kernel width $h = 2 \times 10^{-3}$. Indexes of modes correspond to Table 3; marker shapes are used to indicate memberships in primary clusters of interest classified according to their oscillation periods P ; underlined labels correspond to growing modes. Left panel omits *non-persistent* modes (46). Rectangles indicates modes collected into five different reduced order models (see Section 4.4), comprising, respectively, 13, 25, 65, 46 and 98 modes, amounting to approximately 9, 17, 45, 32, and 69 percent of the rank of the data matrix.

the origin of the coordinate system are neither robustly estimated nor norm-significant and would be likely discarded.

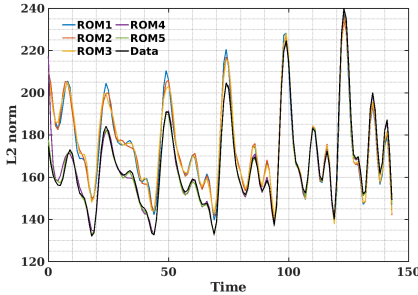
The structure of spatial profiles Φ can be investigated in other ways; for example, [58] clarifies the importance of the total variation norm (the norm of the spatial gradient) of Φ in identification of primary modes. We leave the pursuit of such analyses to a follow-up publication.

4.4. Low-rank model of simulated data

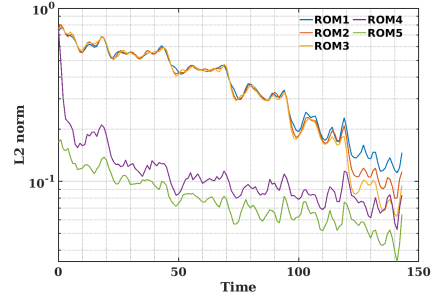
To compare several different reduced-order models (ROMs) of data we retained the modes as indicated by rectangles in Figure 12. The rectangles were chosen based on natural separation of modes in groups on these graphs, although certainly more sophisticated criteria could be formulated, including various clustering techniques and other data mining methods.

The dimensions of ROMs are respectively 13, 25, 65, 46 and 98 modes, amounting to approximately 9, 17, 45, 32, and 69 percent of the rank of the data. ROMs 1–3 include only persistent modes, in the sense of (46), while ROMs 4 and 5 include all modes within the indicated rectangles.

Figure 13 shows norms of low-rank approximations (reduced-order models, ROMs) to the data and norms of differences between data \mathbf{X} and each ROM $\hat{\mathbf{X}}$. It is clear that all ROMs, despite the wide range of their orders, capably reproduce bulk properties (norm) of the data in the latter part of the time domain. The clear difference between ROMs 1–3 and 4–5 is in the transient part; this is expected, since ROMs 1–3 intentionally used only



(a) ℓ^2 norms of snapshots $\|\mathbf{X}[n]\|_2$ and each of the reduced-order models $\tilde{\mathbf{X}}[n]$.



(b) ℓ^2 norms of differences between ROMs and original data $\|\mathbf{X}[n] - \tilde{\mathbf{X}}[n]\|_2 / \|\mathbf{X}[n]\|_2$

Figure 13: Quality of approximation of the original data set $\mathbf{X}[n]$ using each of the reduced-order modes $\tilde{\mathbf{X}}[n]$ corresponding to selections indicated in Figure 12.

the modes that have a relatively-slow decay rate, or are growing. Within the two classes of ROMs (persistent-only and full), the differences are minor even though the dimension of ROMs vary considerably within each class.

5. Connections between modes and oceanographic features

In the following subsections, we highlight connections between oceanographic features and modes, or groups of modes, isolated by the DMD analysis. In particular, we focus on the most persistent dominant modes, enclosed in “ROM 1” box in Figure 12, and listed in Table 4, as these are the most reliably computed features that are observable over the duration of the simulation.

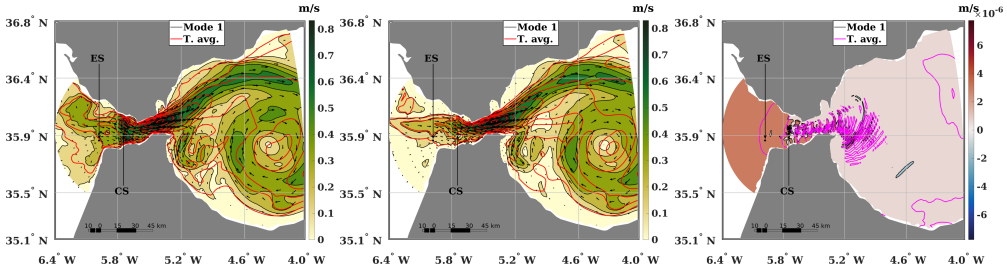
Index	Cluster	Period	Halving (-)/ Doubling (+) Time	RMS \tilde{b}_n	$w\tilde{b}_n$	Robustness $d_h(\lambda_n)$
1	1	Inf	-1078.97	157.02	0.74	282.78
2	3	12.34	-84.48	75.46	1.05	181.47
6	3	12.12	-1029.16	69.55	0.94	190.64
11	2	24.34	-112.00	33.99	0.37	236.18
16	2	26.04	-53.05	19.28	0.32	217.63
24	5	6.19	+90.93	11.11	0.22	199.52
30	4	8.26	-2531.05	9.29	0.20	210.09

Table 4: Properties of DMD modes included in the “ROM 1” reduced order model. Only one conjugate is listed for each complex mode pair. Robustness is estimated using kernel width $h = 2 \times 10^{-3}$. Clusters were assigned based on level sets of kernel density estimates with $h = 2.5 \times 10^{-2}$; Listed modes are a subset of the modes in Table 3.

5.1. Western Alboran Gyre and secondary gyres

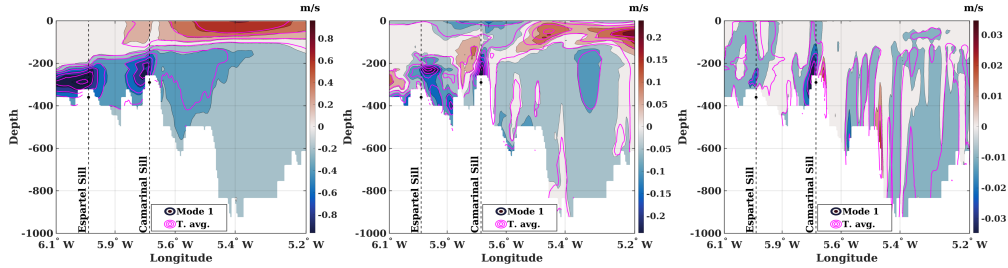
Mode 1 is an aperiodic, near-constant mode that captures the largest proportion of the time-averaged norm of data. For this reason, we expect it to show flow features similar to the time-averaged data, displayed in Figure 6. Figure 14 and Figure 15 show that this is largely the case: the filled-in contours of Mode 1 align with overlaid contours of the time-averaged data. The agreement pertains to both the horizontal circulation, the vertical structure of the exchange flow within the strait, and even the qualitative structure of stationary internal waves created by flow over topographic features.

The only major difference between time-averaged data and the Mode 1 is in the region immediately southwest of the Strait, off the Peninsula de Almina (Ceuta). In this region the outer edge of the anticyclonic Western Alboran Gyre reverses direction and continues to flow down African coast. Mode 1 shows that a secondary counter-clockwise gyre sets up as a result of the flow reversal in this region. The time-averaged velocity field does show increased flow intensity in that region, but it is not apparent from the flow direction in Figure 6 that the flow is organized in a gyre, rather than a hairpin pattern.



(a) Horizontal velocity field; heatmap is the local speed (U_s). The contours is the magnitude of the horizontal velocity. (b) Horizontal velocity field; heatmap is the time average of data, $S_{\bar{U}}$, before applying DMD. (c) Vertical velocity, showing mean upwelling (red) and downwelling (blue) regions. The contours in red show the time average of data, U_z , before applying DMD.

Figure 14: Surface velocities captured by the near-constant Mode 1. For comparison, contours of time averages of the same quantities of data before applying DMD (see Figure 6) are given in red/magenta.



(a) Mode 1 zonal velocity (U_x). (b) Mode 1 meridional velocity (U_y). (c) Mode 1 vertical velocity component. Contours (in magenta) are the time-averages of the same quantity. Contours (in magenta) are the average of the same quantity. Contours (in magenta) are the time-average of the same quantity.

Figure 15: Mode 1 velocity components along the vertical slice (see Figure 1) through the region. For comparison, time averages of the same quantities (see Figure 4) are given as contours.

5.2. Oscillation inside the Strait

Modes 2 and 6 in Table 4, with respective periods of 12.34h and 12.12h are both approximately semidiurnal, with the dominant activity inside the Strait of Gibraltar, corresponding well to the choice of the semidiurnal tidal components in the forcing of the model Table 2. These modes are associated with a modulation of the horizontal velocity that is predominantly longitudinal, as evidenced by the horizontal tidal ellipses (Figures 16a and 16b). The horizontal direction of surface flow in both components reverses around the Camarinal sill (CS), where also the semidiurnal vertical flow is the strongest (Fig. 17). The inversion of the surface tidal current at CS can be attributed to the different nature of the semidiurnal tides at either side of sill: west of CS and over CS itself tides are mostly barotropic (Tsimplis 2000), whereas east of CS tides have a stronger baroclinic structure (Fig. 17a,b). This baroclinic character stems from the eastward radiation of internal waves from the CS, some of which in the form of (short) solitary waves (Fig. 16 e,f).

Modes 11 and 16 are both approximately diurnal, with respective periods of 24.34h and 26.04h. While mode 11 could be harmonically related to the mode 6 (as $24.34 \approx 2 \times 12.12$), mode 16 is unlikely a harmonic of either modes 2 or 6. The tidal ellipses of the horizontal velocity for these modes are rounder, being near-circular in the western part of the strait, suggesting that they are responsible for some meandering of the motion through the strait. Vertical motion associated with these modes seems to be more active on the east side of the strait, potentially corresponding to the dynamics of the waves originating at the hydraulic jump of the Camarinal sill and propagating into the Mediterranean. Vertical flow pattern of these modes suggests that there is a three-dimensional corkscrew structure embedded in the strait, as upwelling and downwelling regions.

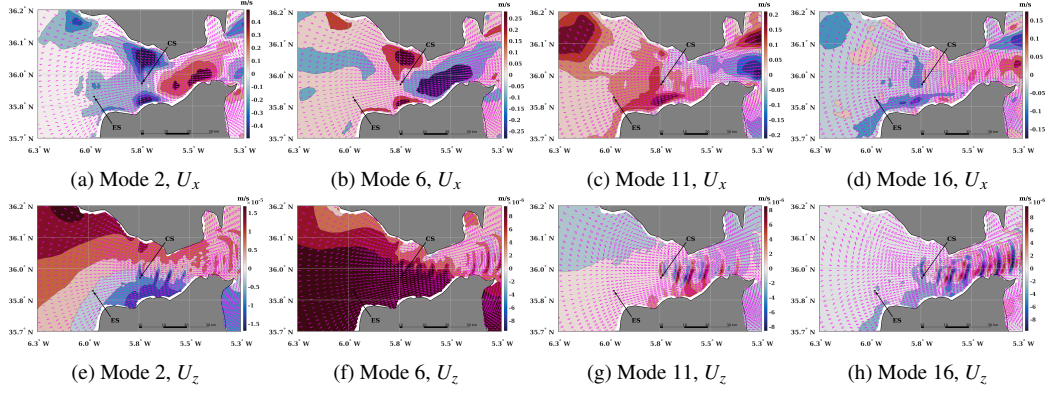


Figure 16: Horizontal longitudinal component U_x (top row) and vertical velocity U_z (bottom row) components of the semidiurnal modes (2 and 6) and diurnal modes (11 and 16).

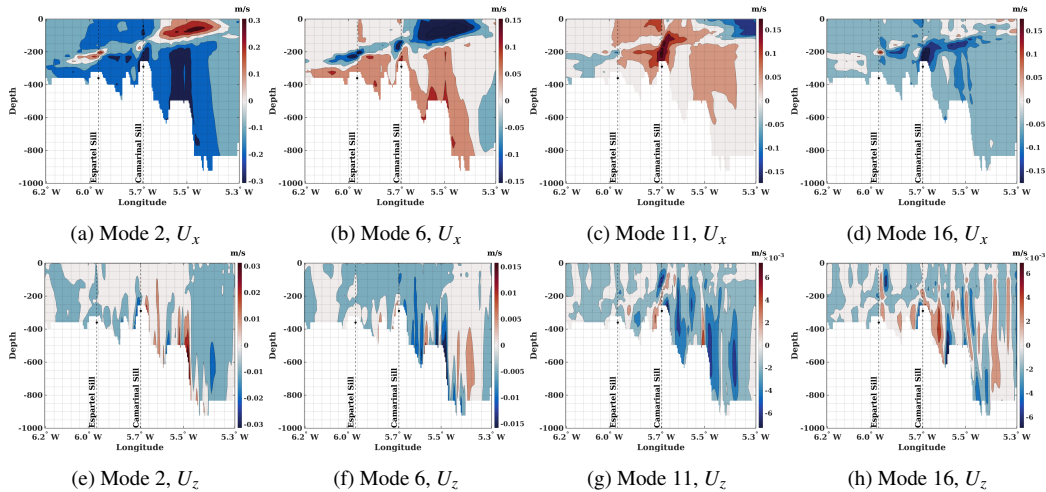


Figure 17: Real part of the longitudinal U_x and vertical U_z velocity components. The semidiurnal modes (2 and 6) show that the two layers of water moving through the strait alternate directions every 12 hours, while the diurnal modes (11 and 16) account for variation in the dominant direction of the flow in the surface and sub-surface layers, respectively.

5.3. Meanders in the Atlantic Jet

Modes 11 and 16 are roughly-diurnal modes that are decaying over the duration of the simulation (Mode 16 decays at roughly twice the rate of Mode 11). We associate these modes with meanders in the Atlantic Jet because their velocity field at the surface is perpendicular to the mean movement of the Atlantic jet along the European Mediterranean coast, as shown in Figure 18.

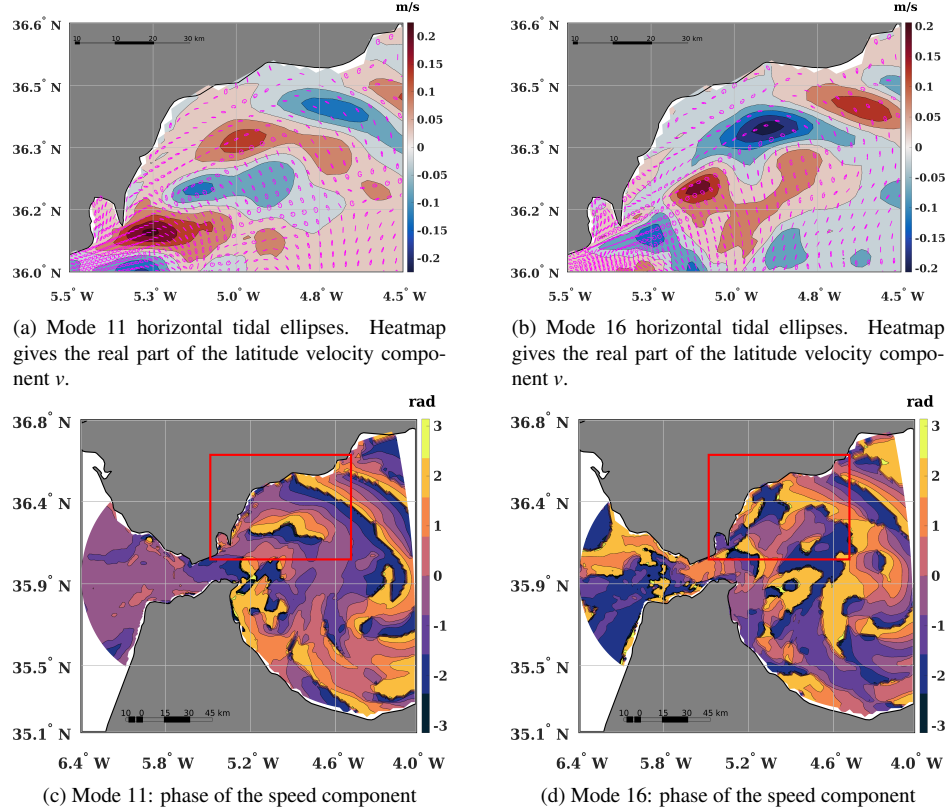


Figure 18: Comparison of the diurnal Modes 11 and 16. The tidal ellipses demonstrate that these modes capture the meanders in the Atlantic jet, that is the oscillation perpendicular to the mean movement of the jet. The parallel phase lines indicate the region where the mode propagates as a wavefront. Frames in the bottom row correspond to the boundaries of the plots in the top row.

The phase lines of each mode connect the geographical locations that simultaneously experience the peaks of the speed under each mode. They can be used to infer the speed of spatial propagation of the modal crest across the domain, as the travel time is exactly one period of oscillation between two isolines of the same phase angle value. Parallel phase lines indicate a geographical region where the mode is propagating as a wavefront, traveling perpendicularly to the phase line. It can be seen in the bottom row of Figure 18 that Mode 11 captures the wavefront of the disturbance that moves across the entire length

of the Atlantic Jet at a speed of about 30 km/day. Mode 16 on the other hand has a much more disorganized phase immediately to the east of the Strait; however, it also organizes as a traveling front further along the coast of Spain.

5.4. Kelvin waves along the African coast

Kelvin and other coastal-trapped waves can propagate along coastlines and can do so for long distances without losing their energy. In the Northern Hemisphere, these waves tend to propagate with the coastline to the right of their propagation direction. Near-diurnal modes 11 and 16, with periods of 24.34 and 26.04 hours respectively, contain some features of coastal-trapped wave propagation. The surface tidal ellipses for mode 11 tend to be elongated near the African coast, with a tendency in some locations to align along the coast (Fig. 11a) (A Kelvin wave would have zero onshore velocity and therefore tidal ellipses that would be flat and parallel to the coast.) The phase speed of Mode 11, estimated from the phase distribution along the coast (Fig. 11c) is approximately 1m/s, which is close the theoretical estimate. The latter is taken as the speed of a long, first-vertical mode gravity wave speed, calculated as $c = \{g'h_1h_2/(h_1 + h_2)\}^{1/2}$, where $g' = 0.015\text{m/s}^{-2}$ is the reduced gravity and $h_1 = 100\text{m}$, $h_2 = 200\text{m}$ are representative values of the Atlantic and Mediterranean layers thickness over the African slope, respectively, derived from the mean stratification. In addition, the velocity magnitude of mode 11 is generally strongest within a Rossby radius of deformation, here about 30 km, of the coastline. It would thus appear that mode 11 contains at least some characteristics of a Kelvin wave propagating eastward along the coast of Africa. Mode 16 also exhibits a degree of coastal trapping (Fig. 19b), but here the tidal ellipses are rounder and the phase distribution (Fig. 19d) is more complex, making it more difficult to compute an along-coast phase speed. For both modes, the off-shore phase distribution is quite complex, no surprising in view of the presence of offshore topographic features. These modes were the two most robustly computed DMD modes, with respect to the leave-one-out analysis, except for the time-invariant mode (Section 4.2). Figures Figure 19 and Figure 20 show the modes at the surface and at the 37.5 ppm mean-isohaline (Figure 7).

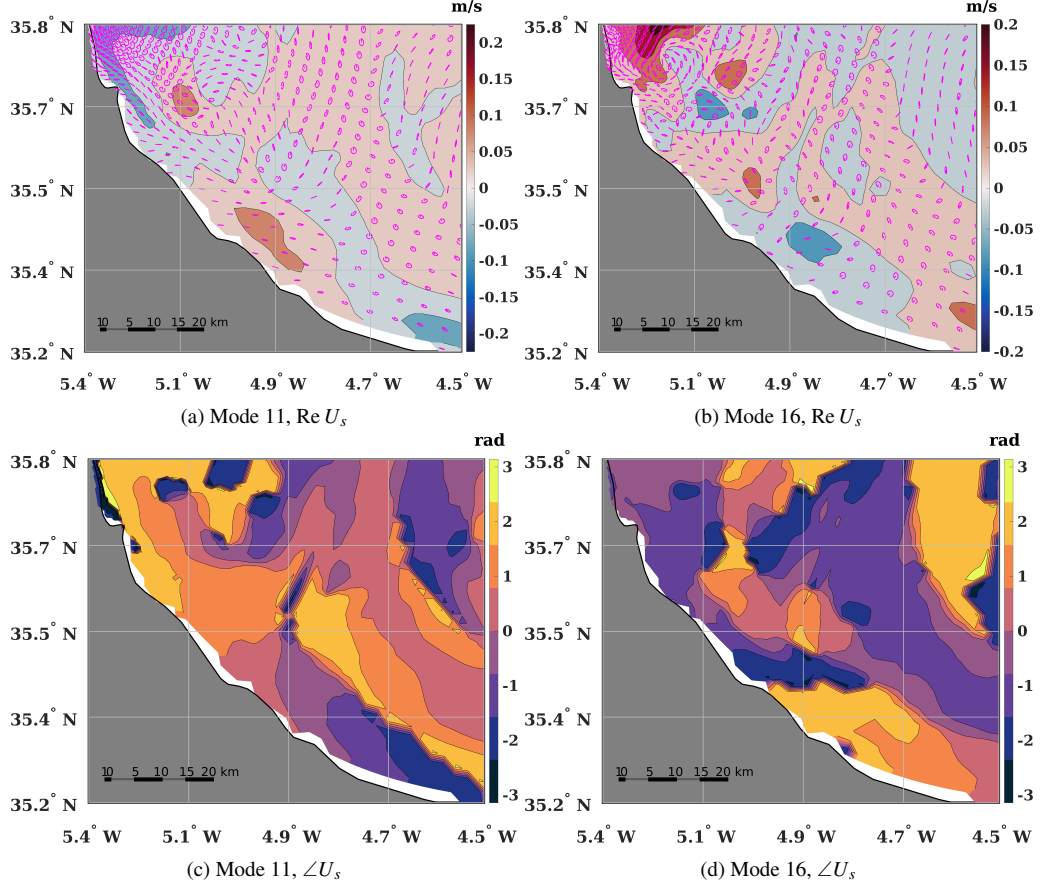


Figure 19: Near-diurnal modes 11 and 16 visualized at the surface layer, along the African coast of the Alboran sea. Top row: tidal ellipses of the horizontal velocity component; heat map represents the modes contribution to the horizontal speed. Bottom row: phase of the speed component. The eight adjacent phase lines are mapped into each other every $\approx 24\text{hr}/8 = 3\text{hr}$ approximately.

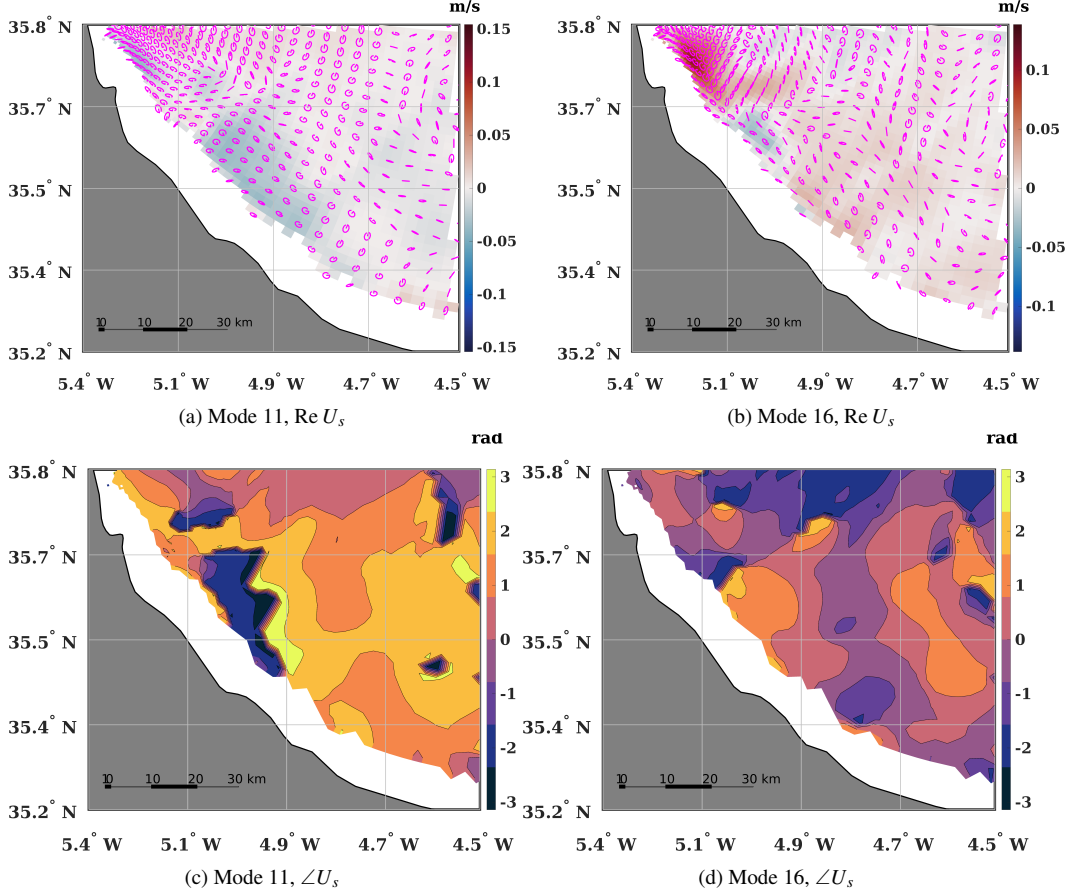


Figure 20: Near-diurnal modes 11 and 16 slices at 37.5 ppm mean-isohaline, along the African coast of the Alboran sea. Top row: tidal ellipses are generated based on the horizontal velocity components; heat map is the modes contribution to the horizontal speed. Bottom row: phase of the speed component. The eight adjacent phase lines are mapped into each other every $\approx 24\text{hr}/8 = 3\text{hr}$ approximately.

6. Discussion and conclusions

The primary objective of this paper is to assess the efficacy of applying DMD to an oceanic region characterized by a diverse array of time-dependent, three-dimensional physical phenomena, including waves, eddies, and gyres, some of which stem from highly non-linear processes. We aim to evaluate how effectively the Koopman modes capture known features and whether the method can unveil previously undiscovered elements within the data. Additionally, we are interested in ranking the numerous computed modes and determining the potential for order reduction.

As a side objective, we sought to demonstrate the application of DMD to the dataset in a clear and straightforward manner. This aspect is essential as it facilitates the wider adoption of this methodology within the scientific community. Our modifications to the algorithm aimed to enhance its numerical performance and efficiency, ensuring that it can be effectively applied to real-world oceanic datasets. These modifications included the incorporation of horizontal speed as an observable in the snapshot vector, the impact of mean value removal during pre-processing, and the introduction of the total-least-squares (TLSQ). Notably, our findings reveal that omitting mean removal results in improved approximation quality for non-constant modes, attributed to the orthogonality of DMD modes. Furthermore, the introduction of the TLSQ correction as a solution to biases in eigenvalues in the baseline DMD algorithm, enhance the accuracy of the data representation. These enhancements contribute to the broader goal of making advanced data analysis techniques more accessible to researchers and practitioners in the field of oceanography.

When interpreting our results, it became evident that while DMD is a powerful tool for data analysis, some limitations need to be considered. The selection of the parameter “ r ” in Singular Value Decomposition (SVD) for DMD was a critical consideration, as it directly impacted the number of modes and the quality of our results. Through thorough analysis, we found that striking the right balance between capturing relevant modes and minimizing noise is the key to this selection process. Additionally, we explored the robustness of eigenvalues estimated using an efficient algorithm that employed linear regression on pairs of snapshots. Here, we investigated the behavior of DMD eigenvalues when snapshots are omitted and the implications of limited data. To assess the robustness, a leave-one-out analysis is conducted, involving repeated eigenvalue computation while randomly excluding snapshots. The results are used to create Kernel Density Estimates (KDE) on the complex plane to visualize eigenvalue distributions. The analysis reveals eigenvalue clusters related to tidal components, with some showing greater robustness than others. Eigenvalues near the unit circle are also discussed in the context of finite data. Figures and a summary table provide a visual and quantitative analysis of the findings.

Our finding also have implication of the ability to rank DMD modes and propose various criteria for their assessment is a valuable contribution. These criteria, such as the ℓ^2 -norm and RMS norms, provide a framework for researchers to evaluate and compare modes in future studies. The discussion of mode contributions to initial conditions and their RMS

contributions is particularly illuminating. This approach offers a practical means to discern between modes with varying impact, providing researchers with tools to prioritize relevant modes for their analyses.

Our findings also have broader implications for the field of oceanography. Our study's results aligned with existing oceanography literature in the field, providing a foundation for further exploration. In particular, our findings complemented previous research related to oceanic processes, enhancing our understanding of these phenomena. This conformity with existing knowledge reinforces the validity of our methodology and highlights its potential for broader adoption in oceanography. Additionally, this involves unveiling previously undiscovered oceanographic features using the dataset.

Our findings explain by DMD Mode 1's association with oceanographic characteristics, notably the Western Alboran Gyre. Mode 1, an aperiodic and relatively constant mode, closely resembles the time-averaged data in terms of horizontal and vertical flow patterns and the formation of stationary internal waves. However, a notable distinction arises in the region southwest of the Strait, near the Peninsula de Almina, where Mode 1 reveals the development of a secondary counter-clockwise gyre due to flow reversal. This observation is less apparent in the time-averaged data, emphasizing the utility of DMD analysis, particularly Mode 1, in uncovering valuable insights into the Western Alboran Gyre and associated oceanographic features.

Additionally this study analyzed the oscillatory modes within the Strait of Gibraltar. It identifies semidiurnal DMD Modes 2 and 6, associated with longitudinal modulation of horizontal velocity, impacting the strait's dynamics, particularly around the Camarinal sill. The inversion of surface tidal currents at the Camarinal sill is attributed to differences in tidal characteristics on either side. Additionally, the study observes diurnal Modes 11 and 16, influencing horizontal motion and promoting meandering within the strait, with more pronounced vertical motion on the eastern side. These modes suggest a three-dimensional corkscrew-like structure within the strait, involving upwelling and downwelling regions. The findings provide valuable insights into the complex dynamics of the Strait of Gibraltar, encompassing both semidiurnal and diurnal behaviors and their influence on horizontal and vertical flows.

Furthermore, DMD Modes 11 and 16, which exhibit diurnal characteristics, were investigated in the context of meanders within the Atlantic Jet. Mode 16 was observed to decay at a rate approximately twice that of Mode 11. These modes were associated with meandering patterns in the Atlantic Jet, as indicated by their surface velocity fields perpendicular to the jet's typical movement along the European Mediterranean coast. Phase lines connecting geographical locations with simultaneous speed peaks under each mode were used to infer the spatial propagation characteristics. Notably, Mode 11 exhibited a well-defined waveform, traveling at a speed of around 30 km/day across the entire length of the Atlantic Jet. Conversely, Mode 16 initially displayed disorganized behavior but eventually organized into a traveling front along the coast of Spain. These insights, illustrated in Figure 18, contribute to a deeper understanding of the Atlantic Jet's dynamics, particularly its

meandering phenomena and the complex interactions within this oceanic system.

This study also investigated the propagation of Kelvin and coastal-trapped waves along the African coast, focusing on two specific DMD modes, Mode 11 and Mode 16. Mode 11 shows features of a Kelvin wave, with elongated tidal ellipses near the African coast and a phase speed in agreement with theoretical estimates. The velocity magnitude of Mode 11 is strongest within a certain distance from the coastline, indicating its coastal nature. Mode 16 exhibits some coastal trapping characteristics but with rounder tidal ellipses and a complex phase distribution due to offshore topographic features. These findings are visually depicted in Figures 19 and 20, providing insights into the modes' behavior at the surface and at a specific isohaline level along the African coast.

In summary, this study presents a comprehensive analysis of the application of DMD to complex oceanic data. Our findings demonstrate the potential for DMD to unlock valuable insights within dynamic, multidimensional datasets and underscore the importance of carefully considering preprocessing steps and parameter choices. This work contributes to the broader objective of making advanced data analysis methods accessible to a wider scientific audience, with implications for oceanography and related fields.

7. Acknowledgments

Some of the computing for this project was performed on the Clarkson University ACRES cluster. We would like to thank Clarkson University Office of Information Technology, and the National Science Foundation, who partially funded these resources under Grant No. 1925596.

References

- [1] P. J. Schmid, Dynamic mode decomposition of numerical and experimental data, *Journal of Fluid Mechanics* 656 (2010) 5–28. doi:10.1017/S0022112010001217.
- [2] C. W. Rowley, I. Mezić, S. Bagheri, P. Schlatter, D. S. Henningson, Spectral analysis of nonlinear flows, *Journal of Fluid Mechanics* 641 (2009) 115–127. doi:10.1017/S0022112009992059.
- [3] T. R. Smith, J. Moehlis, P. Holmes, Low-Dimensional Modelling of Turbulence Using the Proper Orthogonal Decomposition: A Tutorial, *Nonlinear Dynamics* 41 (1-3) (2005) 275–307. doi:10.1007/s11071-005-2823-y.
- [4] E. N. Lorenz, Empirical orthogonal functions and statistical weather prediction (1956).
- [5] B. C. Weare, J. S. Nasstrom, Examples of Extended Empirical Orthogonal Function Analyses, *Monthly Weather Review* 110 (6) (1982) 481–485. doi:10.1175/1520-0493(1982)110<0481:EOEOF>2.0.CO;2.

- [6] K. Taira, M. S. Hemati, S. L. Brunton, Y. Sun, K. Duraisamy, S. Bagheri, S. T. M. Dawson, C.-A. Yeh, Modal Analysis of Fluid Flows: Applications and Outlook, *AIAA Journal* 58 (3) (2020) 998–1022. doi:10.2514/1.J058462.
- [7] K. Taira, S. L. Brunton, S. T. M. Dawson, C. W. Rowley, T. Colonius, B. J. McKeon, O. T. Schmidt, S. Gordeyev, V. Theofilis, L. S. Ukeiley, Modal Analysis of Fluid Flows: An Overview, *AIAA Journal* 55 (12) (2017) 4013–4041. doi:10/gdh7zw.
- [8] I. Mezić, A. Banaszuk, Comparison of systems with complex behavior, *Physica D. Nonlinear Phenomena* 197 (1-2) (2004) 101–133. doi:10.1016/j.physd.2004.06.015.
- [9] I. Mezić, Spectral properties of dynamical systems, model reduction and decompositions, *Nonlinear Dynamics. An International Journal of Nonlinear Dynamics and Chaos in Engineering Systems* 41 (1-3) (2005) 309–325. doi:10.1007/s11071-005-2824-x.
- [10] M. Korda, I. Mezić, On Convergence of Extended Dynamic Mode Decomposition to the Koopman Operator, *Journal of Nonlinear Science* 28 (2) (2018) 687–710. arXiv: 1703.04680, doi:10.1007/s00332-017-9423-0.
- [11] M. Korda, I. Mezić, Linear predictors for nonlinear dynamical systems: Koopman operator meets model predictive control, *Automatica* 93 (2018) 149–160. doi:10.1016/j.automatica.2018.03.046.
- [12] I. Mezić, Analysis of Fluid Flows via Spectral Properties of the Koopman Operator, *Annual Review of Fluid Mechanics* 45 (1) (2013) 357–378. doi:10/gcvjw4.
- [13] I. Mezić, Spectrum of the Koopman Operator, Spectral Expansions in Functional Spaces, and State-Space Geometry, *Journal of Nonlinear Science* (Dec. 2019). doi: 10.1007/s00332-019-09598-5.
- [14] S. L. Brunton, M. Budišić, E. Kaiser, J. N. Kutz, Modern Koopman Theory for Dynamical Systems, arXiv:2102.12086 [cs, eess, math] (Feb. 2021). arXiv:2102.12086.
- [15] M. Budišić, R. Mohr, I. Mezić, Applied Koopmanism, *Chaos. An Interdisciplinary Journal of Nonlinear Science* 22 (4) (2012) 047510, 33. doi:10.1063/1.4772195.
- [16] A. Mauroy, I. Mezic, Y. Susuki (Eds.), *The Koopman Operator in Systems and Control: Concepts, Methodologies, and Applications*, Lecture Notes in Control and Information Sciences, Springer International Publishing, 2020. doi:10.1007/978-3-030-35713-9.

- [17] R. Pawlowicz, B. Beardsley, S. Lentz, Classical tidal harmonic analysis including error estimates in MATLAB using T_TIDE, *Computers & Geosciences* 28 (8) (2002) 929–937. doi:10.1016/S0098-3004(02)00013-4.
- [18] M. G. G. Foreman, R. F. Henry, The harmonic analysis of tidal model time series, *Advances in Water Resources* 12 (3) (1989) 109–120. doi:10.1016/0309-1708(89)90017-1.
- [19] J. C. Sánchez-Garrido, J. G. Lafuente, E. Á. Fanjul, M. G. Sotillo, F. J. de los Santos, What does cause the collapse of the western alboran gyre? results of an operational ocean model, *Progress in Oceanography* 116 (2013) 142–153.
- [20] H. Lacombe, C. Richez, The regime of the Strait of Gibraltar, in: Elsevier Oceanography Series, Vol. 34, Elsevier, 1982, pp. 13–73.
- [21] L. Armi, D. M. Farmer, The flow of Mediterranean water through the strait of Gibraltar. The flow of Atlantic water through the Strait of Gibraltar, *Progress in Oceanography* 21 (1) (1988) 1–105.
- [22] L. Armi, D. Farmer, The internal hydraulics of the Strait of Gibraltar and associated sills and narrows, *Oceanologica Acta* 8 (1) (1985) 37–46.
- [23] J. Wesson, M. Gregg, Turbulent dissipation in the Strait of Gibraltar and associated mixing, in: Elsevier Oceanography Series, Vol. 46, Elsevier, 1988, pp. 201–212.
- [24] F. Boyce, Internal waves in the Straits of Gibraltar, in: Deep Sea Research and Oceanographic Abstracts, Vol. 22, Elsevier, 1975, pp. 597–610.
- [25] J. Ziegenbein, Short internal waves in the Strait of Gibraltar, in: Deep Sea Research and Oceanographic Abstracts, Vol. 16, Elsevier, 1969, pp. 479–487.
- [26] G. Watson, I. Robinson, A study of internal wave propagation in the Strait of Gibraltar using shore-based marine radar images, *Journal of Physical Oceanography* 20 (3) (1990) 374–395.
- [27] N. Pettigrew, R. Hyde, The structure of the internal bore in the Strait of Gibraltar and its influence on the Atlantic inflow, in: *The Physical Oceanography of Sea Straits*, Springer, 1990, pp. 493–508.
- [28] C. Richez, Airborne synthetic aperture radar tracking of internal waves in the Strait of Gibraltar, *Progress in Oceanography* 33 (2) (1994) 93–159.
- [29] W. Alpers, P. Brandt, A. Rubino, J. O. Backhaus, Recent contributions of remote sensing to the study of internal waves in the straits of Gibraltar and Messina, *BULLETIN-INSTITUT OCEANOGRAPHIQUE MONACO-NUMERO SPECIAL-* (1996) 21–40.

[30] P. Brandt, W. Alpers, J. O. Backhaus, Study of the generation and propagation of internal waves in the Strait of Gibraltar using a numerical model and synthetic aperture radar images of the European ERS 1 satellite, *Journal of Geophysical Research: Oceans* 101 (C6) (1996) 14237–14252.

[31] J. R. Apel, P. F. Worcester, Internal solitons near Gibraltar: A longitudinal study using ERS-1 & 2 SAR imagery, in: *ESA ERS-ENVISAT Symposium” Looking down to Earth in the New Millennium”* (Gothenburg, Sweden), ESA Paper SP461, Citeseer, 2000.

[32] J. Apel, Solitons near Gibraltar: Views from the European remote sensing satellites. Report GOA 2000–1, Global Ocean Association, Silver Spring, MD (2000).

[33] J. C. Sánchez-Garrido, G. Sannino, L. Liberti, J. G. Lafuente, L. Pratt, Numerical modeling of three-dimensional stratified tidal flow over Camarinal Sill, Strait of Gibraltar, *Journal of Geophysical Research: Oceans* 116 (C12) (2011). doi: 10.1029/2011JC007093.

[34] J. Marshall, A. Adcroft, C. Hill, L. Perelman, C. Heisey, A finite-volume, incompressible navier stokes model for studies of the ocean on parallel computers, *Journal of Geophysical Research: Oceans* 102 (C3) (1997) 5753–5766. arXiv:<https://agupubs.onlinelibrary.wiley.com/doi/pdf/10.1029/96JC02775>, doi:10.1029/96JC02775.

[35] J. C. Sánchez-Garrido, J. G. Lafuente, E. Álvarez Fanjul, M. G. Sotillo, F. J. de los Santos, What does cause the collapse of the western alboran gyre? results of an operational ocean model, *Progress in Oceanography* 116 (2013) 142 – 153. doi:10.1016/j.pocean.2013.07.002.
URL <http://www.sciencedirect.com/science/article/pii/S0079661113001080>

[36] J. C. Sánchez-Garrido, C. Naranjo, D. Macías, J. García-Lafuente, T. Oguz, Modeling the impact of tidal flows on the biological productivity of the alboran sea, *Journal of Geophysical Research: Oceans* 120 (11) (2015) 7329–7345. arXiv:<https://agupubs.onlinelibrary.wiley.com/doi/pdf/10.1002/2015JC010885>, doi: 10.1002/2015JC010885.

[37] W. G. Large, J. C. McWilliams, S. C. Doney, Oceanic vertical mixing: A review and a model with a nonlocal boundary layer parameterization, *Reviews of Geophysics* 32 (4) (1994) 363–403. arXiv:<https://agupubs.onlinelibrary.wiley.com/doi/pdf/10.1029/94RG01872>, doi:10.1029/94RG01872.

[38] J. Smagorinsky, General circulation experiments with the primitive equations: I. the basic experiment, *Monthly Weather Review* 91 (3) (1963) 99–164. doi:10.1175/1520-0493(1963)091<0099:GCEWTP>2.3.CO;2.

[39] E. Kalnay, M. Kanamitsu, R. Kistler, W. Collins, D. Deaven, L. Gandin, M. Iredell, S. Saha, G. White, J. Woollen, Y. Zhu, M. Chelliah, W. Ebisuzaki, W. Higgins, J. Janowiak, K. C. Mo, C. Ropelewski, J. Wang, A. Leetmaa, R. Reynolds, R. Jenne, D. Joseph, The ncep/ncar 40-year reanalysis project, *Bulletin of the American Meteorological Society* 77 (3) (1996) 437–472. arXiv:[https://doi.org/10.1175/1520-0477\(1996\)077<0437:TNYRP>2.0.CO;2](https://doi.org/10.1175/1520-0477(1996)077<0437:TNYRP>2.0.CO;2), doi:10.1175/1520-0477(1996)077<0437:TNYRP>2.0.CO;2.

[40] M. G. Sotillo, S. Cailleau, P. Lorente, B. Levier, R. Aznar, G. Reffray, A. Amo-Baladrón, J. Chanut, M. Benkiran, E. Alvarez-Fanjul, The myocean ibi ocean forecast and reanalysis systems: operational products and roadmap to the future copernicus service, *Journal of Operational Oceanography* 8 (1) (2015) 63–79. arXiv:<https://doi.org/10.1080/1755876X.2015.1014663>, doi:10.1080/1755876X.2015.1014663.

[41] J. Candela, C. Winant, A. Ruiz, Tides in the Strait of Gibraltar, *Journal of Geophysical Research: Oceans* 95 (C5) (1990) 7313–7335. doi:10.1029/JC095iC05p07313.

[42] J. G. Lafuente, J. Almazán, F. Castillejo, A. Khribache, A. Hakimi, Sea level in the strait of gibraltar: Tides, *The International Hydrographic Review* (1990).

[43] M. Tsimplis, Vertical structure of tidal currents over the Camarinal Sill at the Strait of Gibraltar, *Journal of Geophysical Research: Oceans* 105 (C8) (2000) 19709–19728.

[44] J. C. Sánchez Garrido, J. García Lafuente, F. Criado Aldeanueva, A. Baquerizo, G. Sannino, Time-spatial variability observed in velocity of propagation of the internal bore in the Strait of Gibraltar, *Journal of Geophysical Research: Oceans* 113 (C7) (2008).

[45] A. H. Monahan, J. C. Fyfe, M. H. P. Ambaum, D. B. Stephenson, G. R. North, Empirical Orthogonal Functions: The Medium is the Message, *Journal of Climate* 22 (24) (2009) 6501–6514. doi:10.1175/2009JCLI3062.1.

[46] J. H. Tu, C. W. Rowley, D. M. Luchtenburg, S. L. Brunton, J. N. Kutz, On dynamic mode decomposition: Theory and applications, *Journal of Computational Dynamics* 1 (2) (2014) 391–421. doi:10.3934/jcd.2014.1.391.

[47] A. Laub, Numerical linear algebra aspects of control design computations, *IEEE transactions on automatic control* 30 (2) (1985) 97–108.

[48] Z. Drmač, I. Mezić, R. Mohr, Data Driven Koopman Spectral Analysis in Vandermonde–Cauchy Form via the DFT: Numerical Method and Theoretical Insights, *SIAM Journal on Scientific Computing* 41 (5) (2019) A3118–A3151. doi: 10.1137/18M1227688.

[49] Z. Drmač, I. Mezić, R. Mohr, Data Driven Modal Decompositions: Analysis and Enhancements, *SIAM Journal on Scientific Computing* 40 (4) (2018) A2253–A2285. doi: 10.1137/17M1144155.

[50] M. Stoll, A Krylov–Schur approach to the truncated SVD, *Linear Algebra and its Applications* 436 (8) (2012) 2795–2806. doi:10.1016/j.laa.2011.07.022.

[51] K. K. Chen, J. H. Tu, C. W. Rowley, Variants of Dynamic Mode Decomposition: Boundary Condition, Koopman, and Fourier Analyses, *Journal of Nonlinear Science* 22 (6) (2012) 887–915. doi:10.1007/s00332-012-9130-9.

[52] S. M. Hirsh, K. D. Harris, J. N. Kutz, B. W. Brunton, Centering Data Improves the Dynamic Mode Decomposition, *SIAM Journal on Applied Dynamical Systems* 19 (3) (2020) 1920–1955. arXiv:1906.05973, doi:10.1137/19M1289881.

[53] G. S. Seenivasaharagavan, M. Korda, H. Arbabi, I. Mezić, Mean Subtraction and Mode Selection in Dynamic Mode Decomposition, arXiv:2105.03607 [physics] (Jun. 2021). arXiv:2105.03607.

[54] S. T. M. Dawson, M. S. Hemati, M. O. Williams, C. W. Rowley, Characterizing and correcting for the effect of sensor noise in the dynamic mode decomposition, *Experiments in Fluids* 57 (3) (2016) 42. doi:10.1007/s00348-016-2127-7.

[55] M. S. Hemati, C. W. Rowley, E. A. Deem, L. N. Cattafesta, De-biasing the dynamic mode decomposition for applied Koopman spectral analysis of noisy datasets, *Theoretical and Computational Fluid Dynamics* 31 (4) (2017) 349–368. doi:10/gbqfcj.

[56] M. Gavish, D. L. Donoho, The Optimal Hard Threshold for Singular Values is $4/\sqrt{3}$, *IEEE Transactions on Information Theory* 60 (8) (2014) 5040–5053. doi:10.1109/TIT.2014.2323359.

[57] B. P. Epps, E. M. Krivitzky, Singular value decomposition of noisy data: Noise filtering, *Experiments in Fluids* 60 (8) (2019) 126. doi:10.1007/s00348-019-2768-4.

[58] E. Boltt, Geometric Considerations of a Good Dictionary for Koopman Analysis of Dynamical Systems: Cardinality, 'Primary Eigenfunction,' and Efficient Representation, arXiv:1912.09570 [cs, math] (Mar. 2021). arXiv:1912.09570.

[59] G. Tissot, L. Cordier, N. Benard, B. R. Noack, Model reduction using dynamic mode decomposition, *Comptes Rendus Mécanique* 342 (6-7) (2014) 410–416.

[60] D. T. Crommelin, A. J. Majda, Strategies for Model Reduction: Comparing Different Optimal Bases, *Journal of the Atmospheric Sciences* 61 (17) (2004) 2206–2217. doi: 10.1175/1520-0469(2004)061<2206:SFMRCD>2.0.CO;2.